

Probing Surface Spin Interaction Dynamics using Nitrogen-Vacancy Center Quantum Sensors with High-Fidelity State-Selective Transition Control

by

Zimeng Wang

A thesis
presented to the University of Waterloo
in fulfillment of the
thesis requirement for the degree of
Master of Science
in
Physics

Waterloo, Ontario, Canada, 2017
© Zimeng Wang 2017

I hereby declare that I am the sole author of this thesis. This is a true copy of the thesis, including any required final revisions, as accepted by my examiners.

I understand that my thesis may be made electronically available to the public.

Abstract

As a demand from developing nanotechnology and quantum information technology based on mesoscopic material, quantum sensors with better spatial resolution and sensitivity are required.

However, few material meets the requirements of nanoscale sensors including stability and small size. Single spin of Nitrogen-Vacancy(NV) centers in diamond crystal is one kind of the ideal quantum sensors for magnetometry that has been investigated in recent years. It provides a potential way to study the dynamics in a mesoscopic system with high sensitivity at room temperature. This thesis proposes a theoretical method to realize spin interaction detection based on NV centers on an atomic force-microscopy(AFM) tip. To realize this method, a robust control on NV centers and target electron spins at zero magnetic field is necessary. A pulse control technique for NV centers is proposed to realize transitions between two degenerate states at zero magnetic field, which is an important part of the sensing method. The key to realizing this transition is a circularly polarized microwave pulse generated by two parallel wires. Combined with optimal control techniques, this pulse can achieve a gate fidelity over 99.95% theoretically.

Acknowledgements

I would like to thank my thesis advisor Prof. David Cory first for opening the door to his lab for me. I was only able to complete the work in this thesis under his inspiration and encouragement.

I would also like to thank the NV group who work with me during all my years here. Ian Hincks is always there when I have a question on NV centers, no matter the question is on theory, experiment or programming. Madelaine Liddy arranged the NV meetings which enabled me to keep steps with the frontier of NV researches. She also gave me a lot of advices on making this thesis readable. I cannot thank Razieh Annabestani more for her kind help on my research projects and thesis. She was also the first person to talk to me in the Cory group and gave me valuable advices on how to do researches. Also, I am gratefully to Guanru Feng who took her time to read my thesis through and gave me comments and suggestions.

Finally, I must express my very profound gratitude to my parents for providing me with support and encouragement throughout my years of studying here, especially in the hardest time. This accomplishment would not have been possible without them. Thank you.

Dedication

This is dedicated to the one I love.

Table of Contents

List of Figures	viii
1 Introduction	1
2 Spin Physics of the Nitrogen Vacancy Center in Diamond	3
2.1 Nitrogen Vacancy Centers in Diamond	3
2.1.1 Structure	3
2.1.2 Energy Levels	4
2.2 Optically Detected Magnetic Resonance of NV	9
2.2.1 Microwave Control on NV Centers	10
2.2.2 Continuous Wave ODMR	12
2.2.3 Pulsed ODMR	13
2.3 Confocal Microscope	16
3 NV centers as a Magnetic Sensor of Spin	21
3.1 Dipole-dipole Interaction and Secular Approximation	22
3.1.1 Introduction to Dipole-dipole Interaction	22
3.1.2 Dipole-dipole Interaction under Secular Approximation	22
3.2 Locating an Electron Spin with Two NV centers	25
3.2.1 Estimating the Locating Ability	25
3.2.2 Locating the Target Spin using Maximum Likelihood Estimation	26

4	NV Centers with Mechanical Motion as a Sensor of Thin Films	29
4.1	Thin Film Sensing with NV centers	29
4.2	Use NV Centers with Motion to Identify Spins in the Thin Film	30
4.2.1	Homo-spin Dipolar Interaction Decoupling with a 12-pulse Sequence in the Strong Magnetic Field	32
4.2.2	Hetero-spin Dipolar Interaction Recoupling with Mechanical Motion	35
4.3	Experiment Procedure to Detect the Electron Dipolar Network with NVs with motion	35
5	State-Selective Transitions in NV centers at Zero Field	38
5.1	Single Quantum Transition and Double Quantum Transition at Zero Exter- nal Magnetic Field	39
5.2	Enhance robustness with Optimal Control Theory	41
5.2.1	Generating Selective SQT at Zero Field using Two Parallel Wires .	41
5.2.2	Introduction to Optimal Control Theory and Gradient Ascent Algo- rithm	42
5.2.3	Generating Selective SQT with High Robustness using GRAPE . .	45
5.3	Experiment Design and Progress	45
5.3.1	Experiment Procedure for Testing the State-selective SQT Gate . .	45
5.3.2	Microwave circuits	47
6	Summary and Future Work	51
	References	52

List of Figures

2.1	The chemical structure of NV^- center.	4
2.2	The energy structure of NV centers	6
2.3	(a) and (b) are the simulated CW spectrum without and with $NV-^{14}N$ hyperfine interaction, respectively.	13
2.4	Rabi experiment	14
2.5	Rabi experiment	15
2.6	Ramsey experiment	16
2.7	The simplified model of confocal microscope	17
2.8	The practical confocal microscope	19
3.1	Locating the target spin using MLE	27
4.1	The concept model of the thin film sensor	31
4.2	The 12-pulse sequence and the quartz tuning fork	34
4.3	The scaling factor	36
5.1	Generating circularly-polarized microwave using two parallel wires	41
5.2	The pulse sequences for the AWG output and the corresponding robustness plot	46
5.3	The pulse sequences for the proving experiment	47
5.4	The design of the microwave circuit	48
5.5	The completed microwave circuit board and the produced PCB with two parallel wires	50

Chapter 1

Introduction

Solid electron spins of Nitrogen Vacancy(NV) center in diamond are investigated by many researchers recently[1][2][3][4] as an important platform for quantum information processing, quantum communication and quantum sensing.

NV centers have significant applications in quantum information processing (QIP) because of their long coherence time[5] and efficient optical polarization and read-out[6][7]. Moreover, NV centers can be controlled by microwave at ambient conditions[8]. NV centers with the nearby ^{14}N and ^{13}C nuclear spins have also been explored as quantum registers[9][10]. Progresses on coupling two close NV centers have been made to promote the scalability of this quantum system[11]. Furthermore, spin-photon entanglement[12] as well as photonic coupling[13] are also demonstrated, which make it possible to build a hybrid network with NV centers. Some quantum algorithms and quantum simulations have already been performed on the NV platform, such as Deutsch Jozsa algorithm[14], quantum error correction[15], simulations of topological phase transitions[16], etc..

Another important application of NV centers is quantum sensors. The long coherence time of NV spin states enables its high sensitivity to magnetic field and its atom-scale size makes it suitable for resolving small spatial structure. The dynamic decoupling method developed in the QIP researches even increases the coherence time of NV centers to the order of microseconds at room temperature[17][18], which further promotes the sensitivity of NV sensors. Moreover, NV centers' optical readout and easy control at ambient conditions are also very important in building sensors. These properties make NV centers outstanding quantum sensors in comparison with other state-of-art sensing methods, as shown in Table 1.1. NV centers have been proposed to sense magnetic field[19][20], temperature[21], electric[22] and etc..

	Sensitivity(μ_B)	Resolution	Film Thickness	Environment
NV	0.03	atomic scale	20 nm	ambient conditions
Nano-SQUID	1	500 nm	1 μm	Low temperature
SP-STM	1	atomic scale	20 nm	Low temperature+Vacuum
LTEM	100	10 nm	20 nm	Vacuum
MRFM	1	10 nm	20 nm	Low temperature+Vacuum
Commercial-ESR	10^7	1 mm	1 mm	

Table 1.1: This table shows the sensing properties of NV centers[24], nano-SQUID (superconducting quantum interference device)[25], SP-STM (spin polarized scanning tunneling microscopy)[26], LTEM (Lorentz electron microscopy)[27], MRFM (magnetic resonance force microscopy)[28] and commercial ESR (electron spin resonance). The unit of the sensitivity is the Bohr magneton. 1 μ_B sensitivity means this sensor is able to sense single electron spin. This table shows that NV centers have high sensitivity and spatial resolution at room temperature. But NV centers can only sense shallow spins in the films.

NV centers are also potential suitable sensors for thin films[29]. The fabrication of atomically thin films turns possible as the nanotechnology develops[30]. Molecular monolayer films like Langmuir-Blodgett(LB) films[31] can be grown and deposited on certain materials. The molecular films can capture plenty of nuclear or electron spins in the structure. Therefore, they are proposed to work as a platform of spin-based quantum information processing[32]. Researches have also been done on using the spin network in the thin film to entangle two distant spins[33]. However, the practical application of the thin films in QIP requires characterizing the spin dynamics in the film with atom-scale resolution and single-spin sensitivity, which is challenging especially at ambient conditions. Quantum sensors made of NV centers have the advantages of potentially meeting all those requirements. In this thesis, a spin-mechanical quantum system using NV centers is proposed as a sensor of thin films.

This quantum sensor is built by sticking the NV center spins onto an atomic force microscope(AFM) cantilever. To achieve better sensitivity, NV spins is controlled with specially designed high-fidelity microwave gates. In Chapter 2, I will introduce the physical structure, energy levels and experimental methods of NV centers. In Chapter 3, I will introduce the dipole-dipole interactions and the NV-based magnetometry. In Chapter 4, I propose a practical scheme for studying spins in the thin film using NV centers on an AFM tip. To enhance the sensitivity of this spin-mechanical sensor, a method to generate state-selective transitions of NV centers with high fidelity in the zero field based on optimal control theory(OCT) is investigated in Chapter 5.

Chapter 2

Spin Physics of the Nitrogen Vacancy Center in Diamond

2.1 Nitrogen Vacancy Centers in Diamond

An Nitrogen-Vacancy(NV) center is a point defect in diamond with a symmetry of C_{3v} . NV centers can be produced in labs by different methods. Chemical vapor deposition(CVD)[34] and Nitrogen ion implantation[35] are two of the typical ways. NV centers have been proposed for numerous applications including sensing, quantum information processing and quantum communication. The NV center system is generally easy to employ because of its long coherence time at room temperature, optically initialization and readout method with high visibility, and simple microwave control. Here we review the energy structure and optical properties of NV centers.

2.1.1 Structure

Diamond is a face-centered cubic crystal of carbon atoms. The covalent bonding between the atoms leads to high hardness and high thermal conductivity. When a nitrogen atom substitutes a carbon atom in the diamond lattice, and when there is a vacancy in the nearest site, an NV center is formed. The vector that links the nitrogen atom and the vacancy is the principle axis of the zero field splitting(ZFS)[57]. The NV center has four possible orientations in the diamond crystal: $[111]$, $[\bar{1}\bar{1}\bar{1}]$, $[\bar{1}\bar{1}1]$ and $[1\bar{1}\bar{1}]$.

As shown in Figure 2.1, at the vacancy position, each of the three neighbor carbon atoms

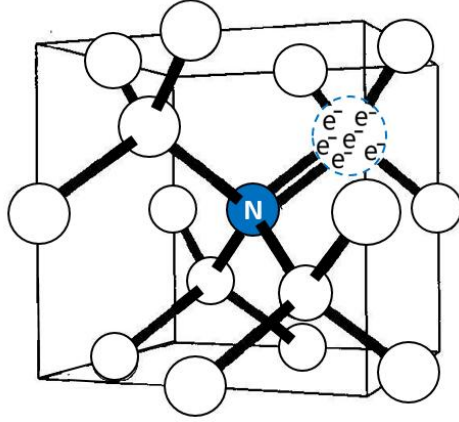


Figure 2.1: The chemical structure of NV^- center.

have a dangling bound that contributes an electron and the nitrogen atom contributes two electrons. Thus, there are five electrons in the neutral NV^0 center. When an extra electron is captured from elsewhere in the lattice, the negative NV^- center is formed. Most single molecule emitters descend to the neutral state after emitting photons in the e^- -poor environment, but NV^- centers bleach to NV^0 with a low probability at room temperature. The focus of this thesis is to study the properties and the applications of NV^- centers.

2.1.2 Energy Levels

Fine Structure and Zeeman Splitting

The six electrons in NV^- can effectively be considered as two spin- $\frac{1}{2}$ particles. Thus NV^- centers are treated as a spin-1 particle. To motivate the effective spin-1 structure of the NV^- center, it is helpful to recall how the exchange interaction takes two distinguishable spin- $\frac{1}{2}$ particles to a singlet/triplet structure[45] when the distinguishability is removed. Consider the exchange interaction between the two spin- $\frac{1}{2}$ particles:

$$H_{exc} = \frac{J}{2}(\sigma_x\sigma_x + \sigma_y\sigma_y) \quad (2.1)$$

where J is the coupling strength between the two particles.
At zero magnetic field,

$$H_{exc} = J \begin{pmatrix} 0 & 0 & 0 & 0 \\ 0 & 0 & 1 & 0 \\ 0 & 1 & 0 & 0 \\ 0 & 0 & 0 & 0 \end{pmatrix}. \quad (2.2)$$

The eigenstates of this Hamiltonian are:

$$\begin{aligned} |\psi_1\rangle &= |\uparrow\uparrow\rangle = |S = 1, m_s = +1\rangle & E_1 &= 0; \\ |\psi_2\rangle &= |\downarrow\downarrow\rangle = |S = 1, m_s = -1\rangle & E_2 &= 0; \\ |\psi_3\rangle &= \frac{|\uparrow\downarrow\rangle + |\downarrow\uparrow\rangle}{\sqrt{2}} = |S = 1, m_s = 0\rangle & E_3 &= -J; \\ |\psi_4\rangle &= \frac{|\uparrow\downarrow\rangle - |\downarrow\uparrow\rangle}{\sqrt{2}} = |S = 0, m_s = 0\rangle & E_4 &= J \end{aligned} \quad (2.3)$$

where S is the total spin angular momentum, m_s is the angular momentum projections on to the z-axis. $|\psi_4\rangle$ is a singlet state with $S = 0$. $|\psi_1\rangle$, $|\psi_2\rangle$, and $|\psi_3\rangle$ are the triplet states with $S = 1$. At zero field, $|\psi_1\rangle$ and $|\psi_2\rangle$ are degenerate; $|\psi_3\rangle$ and $|\psi_{1,2}\rangle$ are separated by J . We denote the corresponding energy eigenvalues of the four states by $\{E_i\}$ ($i = 1, 2, 3, 4$). In a magnetic field $\vec{B} = B_z \hat{z}$, the Hamiltonian of the two spin-half particles are:

$$H_{exc} + \frac{\gamma_e B_z}{2} (\sigma_z \otimes \mathbb{1} + \mathbb{1} \otimes \sigma_z) = \begin{pmatrix} \gamma_e B_z & 0 & 0 & 0 \\ 0 & 0 & J & 0 \\ 0 & J & 0 & 0 \\ 0 & 0 & 0 & -\gamma_e B_z \end{pmatrix}, \quad (2.4)$$

where γ_e is the gyromagnetic ratio of the NV electron spins.

The eigenstates of this Hamiltonian are the same as that of H_{exc} , but their corresponding energy eigenvalues are modified to $\{E'_i\}$ ($i=1,2,3,4$) where:

$$\begin{aligned} E'_1 &= E_1 + \gamma_e B_z, \\ E'_2 &= E_2 - \gamma_e B_z, \\ E'_3 &= E_3, \\ E'_4 &= E_4. \end{aligned} \quad (2.5)$$

The ground state structures with and without the external magnetic field are shown in Figure 2.2(a). In the absence of the external field, there is an energy splitting between $m_s = \pm 1$ and $m_s = 0$ states, which is known as the zero field splitting (ZFS), $\Delta = 2.87$

GHz. In the presence of the field B_z along the NV principle axis, there is an extra splitting between $m_s = \pm 1$ by $2\gamma_e B_z$.

Selection Rules in NV Energy Structure

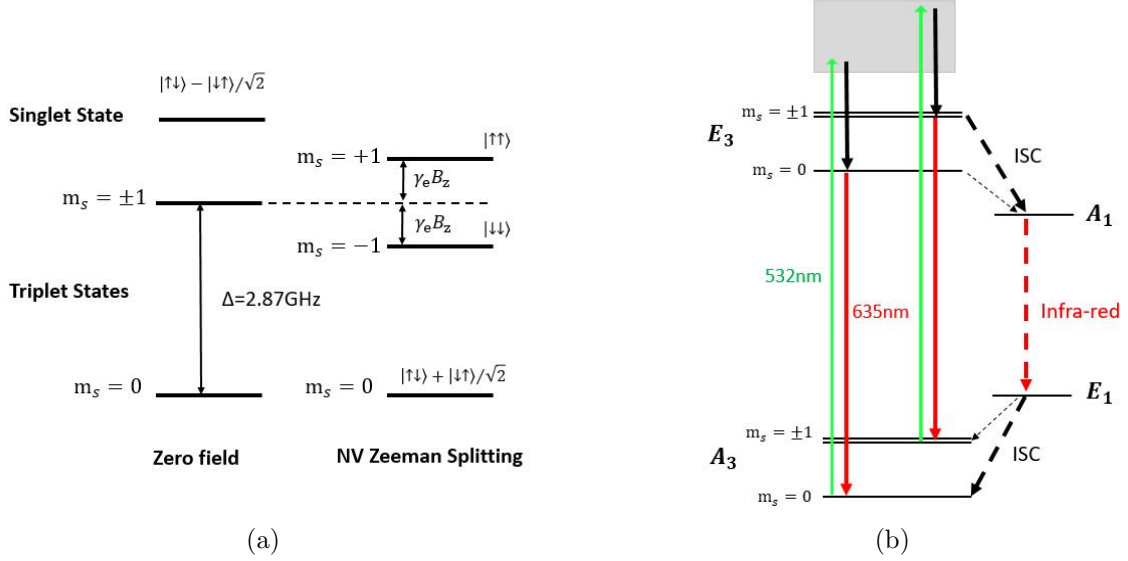


Figure 2.2: (a) The electronic structure of NV ground state. (b) The electronic ground state and excited state with spin allowed transitions.

In the NV electronic structure, some transitions are forbidden by the selection rules. Consider microwave (MW) applied on two electron spins: $H_{mw1} = \Omega(\sigma_x \otimes \mathbb{1} + \mathbb{1} \otimes \sigma_x)$. The amplitude of the MW that the two spin- $\frac{1}{2}$ particles see are the same. According to Fermi's Golden Rule, the transition probability from state $|\psi_i\rangle$ to state $|\psi_j\rangle$ is $2\pi |\langle\psi_f | H_{mw} | \psi_i\rangle|^2$ ($i, j=1, 2, 3, 4$):

$$\begin{aligned}
 \langle\psi_4 | H_{mw1} | \psi_i\rangle &= \langle\psi_i | H_{mw1} | \psi_4\rangle = 0, \quad i=2, 3, 4 \\
 \langle\psi_3 | H_{mw1} | \psi_i\rangle &= \langle\psi_i | H_{mw1} | \psi_3\rangle \neq 0, \quad i=1, 2 \\
 \langle\psi_1 | H_{mw1} | \psi_2\rangle &= \langle\psi_2 | H_{mw1} | \psi_1\rangle = 0
 \end{aligned} \tag{2.6}$$

$|\psi_4\rangle$ is the singlet state, $|\psi_2\rangle$ is the $m_s = 0$ state, and $|\psi_1\rangle$ and $|\psi_3\rangle$ are the $m_s = \pm 1$ states. It shows that the transition between singlet state and the triplet states remains forbidden. Within the triplet states, the transition between $m_s = \pm 1$ states is not allowed but the single quantum transitions between $m_s = 0$ and $m_s = \pm 1$ are allowed under this MW. However, if the two spin- $\frac{1}{2}$ particles are slightly distinguishable: $H_{mw2} = \Omega(\sigma_x \otimes \mathbb{1} + (\mathbb{1} +$

$\epsilon)\mathbb{1} \otimes \sigma_x$), where ϵ is small, and the transition probabilities are:

$$\begin{aligned}
\langle \psi_4 | H_{mw2} | \psi_3 \rangle &= \langle \psi_3 | H_{mw2} | \psi_4 \rangle = 0, \\
\langle \psi_4 | H_{mw2} | \psi_i \rangle &= \langle \psi_i | H_{mw2} | \psi_4 \rangle \neq 0, \quad i=1,2 \\
\langle \psi_3 | H_{mw2} | \psi_i \rangle &= \langle \psi_i | H_{mw2} | \psi_3 \rangle \neq 0, \quad i=1,2 \\
\langle \psi_1 | H_{mw2} | \psi_2 \rangle &= \langle \psi_2 | H_{mw2} | \psi_1 \rangle = 0
\end{aligned} \tag{2.7}$$

The transitions between the singlet state and $m_s = \pm 1$ triplet states are weakly allowed, but the direct transition between $m_s = +1$ and $m_s = -1$ states are still forbidden.

Therefore, in most of the cases, we only consider the triplet subspace of the NV^- , which forms the spin-1 system. However, the weak transitions between triplet and singlet states permit the optical method to prepare and read out the NV states.

NV Center as a Spin-1 System

As analyzed above, the NV^- center is effectively a spin-1 system. Its spin Hamiltonian in a \vec{B} magnetic field is,

$$H = \Delta S_z^2 + \gamma_e \vec{B} \cdot \vec{S}. \tag{2.8}$$

$\vec{S} = (S_x, S_y, S_z)$ are the spin-1 operators:

$$S_x = \frac{1}{\sqrt{2}} \begin{pmatrix} 0 & 1 & 0 \\ 1 & 0 & 1 \\ 0 & 1 & 0 \end{pmatrix}, S_y = \frac{1}{\sqrt{2}} \begin{pmatrix} 0 & -i & 0 \\ i & 0 & -i \\ 0 & i & 0 \end{pmatrix}, S_z = \begin{pmatrix} 1 & 0 & 0 \\ 0 & 0 & 0 \\ 0 & 0 & -1 \end{pmatrix} \tag{2.9}$$

Together with the following operators, the 9 operators form a complete basis set for the 3×3 matrix space:

$$\begin{aligned}
S'_x &= \frac{1}{\sqrt{2}} \begin{pmatrix} 0 & -1 & 0 \\ -1 & 0 & 1 \\ 0 & 1 & 0 \end{pmatrix}, S'_y = \frac{1}{\sqrt{2}} \begin{pmatrix} 0 & -i & 0 \\ i & 0 & i \\ 0 & -i & 0 \end{pmatrix}, S'_z = \begin{pmatrix} 1 & 0 & 0 \\ 0 & 0 & 0 \\ 0 & 0 & 1 \end{pmatrix}, \\
S_m &= \frac{1}{\sqrt{2}} \begin{pmatrix} 0 & 0 & 1 \\ 0 & 0 & 0 \\ -1 & 0 & 0 \end{pmatrix}, S'_m = \frac{1}{\sqrt{2}} \begin{pmatrix} 0 & 0 & 1 \\ 0 & 0 & 0 \\ 1 & 0 & 0 \end{pmatrix}, \mathbb{1} = \frac{1}{\sqrt{3}} \begin{pmatrix} 1 & 0 & 0 \\ 0 & 1 & 0 \\ 0 & 0 & 1 \end{pmatrix}.
\end{aligned}$$

The magnetic field direction is commonly placed along the NV principle axis: $\vec{B} = B_z \hat{z}$. So the NV Hamiltonian can also be simplified to $H = \Delta S_z^2 + \gamma_e B_z S_z$.

Hyperfine interaction

The nitrogen atom in the NV center has a non-zero nuclear spin momentum. ^{15}N atoms are $I = \frac{1}{2}$ nuclear spins with a natural abundance less than 1%; ^{14}N atoms are $I = 1$

nuclear spins with natural abundance larger than 99%. The hyperfine interaction between the nitrogen atom and the electron spin further splits the energy structure.

The hyperfine interaction can be written as $\vec{S} \cdot \mathbf{A} \cdot \vec{I}$ where \mathbf{A} is the hyperfine tensor. The hyperfine interaction consists of two parts: Fermi contact interaction and dipole-dipole interaction between the electron and nuclear spins as introduced in the next section. The Fermi contact interaction is $-\frac{2}{3} \langle \mu_N \mu_e \rangle |\Phi(0)|^2$, where μ_N and μ_e are the nuclear and electron magnetic moments, and $\Phi(0)$ is the electron wavefunction at the nuclear spin. The dipole-dipole interaction is generally written as

$$H_{dip} = \frac{\mu_0 \gamma_1 \gamma_2}{4\pi |\vec{r}|^3} \left(3 \left(\vec{S}_1 \cdot \hat{r} \right) \left(\vec{S}_2 \cdot \hat{r} \right) - \vec{S}_1 \cdot \vec{S}_2 \right). \quad (2.10)$$

γ_i and \vec{S}_i are the gyromagnetic ratio and the spin operator of the i^{th} spin. \vec{r} is the vector point from one spin to the other. $\hat{r} = \vec{r}/|\vec{r}|$ is its unit vector.

For the ^{14}N case, \hat{r} is parallel to the NV principle axis, so the hyperfine tensor \mathbf{A} is diagonal. The NV- ^{14}N Hamiltonian is:

$$H_{NV-^{14}\text{N}} = \Delta S_z^2 + \gamma_e \vec{B} \cdot \vec{S} + \gamma_N \vec{B} \cdot \vec{I} + \vec{S} \cdot \mathbf{A} \cdot \vec{I} + \vec{I} \cdot \mathbf{Q} \cdot \vec{I}. \quad (2.11)$$

The first two terms are the NV Hamiltonian, the third term is the ^{14}N Zeeman term, and the last two terms are the NV- ^{14}N hyperfine interaction and the nuclear quadrupole term respectively. \mathbf{A} is symmetric about the NV-N axis. Its parallel part A_{\parallel} is 2.3 MHz, and its perpendicular part A_{\perp} is 2.1 MHz. The nuclear quadrupole interaction $|Q| = -5.04 \pm 0.05$ MHz is assumed to be diagonal in the principle axis system of the zero field splitting.

The nuclear spin environment around the NV center also includes ^{13}C nuclear spin (1.1% natural abundance) with $I = \frac{1}{2}$ or ^{12}C nuclear spin with $I = 0$. The principal axis of the hyperfine tensor \mathbf{A} s between the electron spin and its surrounding ^{13}C spins are not parallel to \hat{z} in general. The total spin Hamiltonian can be written as:

$$\frac{H_{NV-^{13}\text{C}}}{\hbar} = \Delta S_z^2 + \gamma_e \vec{B} \cdot \vec{S} + \sum_j \left(\gamma_C \vec{B} \cdot \vec{I}_j + \vec{S} \cdot \mathbf{A}_j \cdot \vec{I}_j \right) + \sum_{jk} \vec{I}_j \cdot \mathbf{D}_{j,k} \cdot \vec{I}_k. \quad (2.12)$$

The terms correspond to the NV zero field splitting, NV Zeeman term, ^{13}C Zeeman term, NV- ^{13}C hyperfine interaction and ^{13}C - ^{13}C dipolar interaction, respectively. j is the index of surrounding ^{13}C s.

Optical Transitions

Figure 2.2(b) shows both the excited and ground states with optically allowed transitions of the NV center. At low temperature, these can be observed as transitions at around 637 nm for the triplet and around 1046 nm for the singlet. At higher temperatures, the peaks are broadened by phonon-related processes.

At room temperature, it is common to excite the NV centers by a 532 nm laser to a set of continuous states and it will rapidly fall down to the first electronic excited state E_3 . This process is spin-conserving. To be more specific, NV centers in $m_s = \pm 1$ or 0 in the ground triplet state A_3 will be excited to the second excited state, and rapidly fall to the $m_s = \pm 1$ or 0 state respectively in the E_3 state.

NV centers have two paths to fall back to the ground state from the E_3 state. One is a spin-conserving process that emits one photon at 637 nm wavelength and relaxes back. The other path goes through the excited singlet state A_1 and the ground singlet state E_1 to the ground state emitting infra-red light. This second path is an inter-system crossing (ISC) which does not conserve the spin angular momentum.

From $m_s = 0$ in the E_3 state, the NV spin will mainly directly relax back to the $m_s = 0$ in A_3 state, after a lifetime of around 13 ns in E_3 . From $m_s = +1$ or $m_s = -1$ in the E_3 state, NV will go directly to $m_s = +1$ or $m_s = -1$ in the A_3 state at 2/3 probability. 1/3 of the time, the spin process goes through the ISC to the A_1 and E_1 states, and relaxes to $m_s = 0$ in the A_3 state at a large chance. Therefore, the NV spin tends to fall back to the $m_s = 0$ ground state as a result of this probability difference between the paths that the spin in the E_3 $m_s = \pm 1$ states relaxes through. If these transitions are driven for enough periods, the NV center can be optically initialized to $m_s = 0$ ground state with polarization over 95 %. This process can also be used for readout. To measure the final state of NV centers after a certain experiment, we need to repeat the experiments for multiple times and calculate ratio of the detected photon counts out of the total repeating times. This ratio tells the composition of the detected NV state. There are other interesting NV-related readout methods like single shot readout[36][37], spin-light coherence[38] and etc..

Now we wish to explore how to use this center to study the thin film sample. First we introduce the optically detected magnetic resonance method.

2.2 Optically Detected Magnetic Resonance of NV

Optically detected magnetic resonance (ODMR) is a general method to study the spin structure of certain materials. When applicable, ODMR provides a sensitive method to

study electron or nuclear spins since the photon energy is much higher than the energy of a spin flip.

ODMR can be easily combined with conventional optical imaging method like confocal microscopy as introduced in Section 2.3. ODMR techniques are greatly used in NV center studies and important in realizing spin-based sensors.

In this section, how the microwave controls the NV centers will be introduced. Some basic knowledge about continuous microwave experiments at zero and small external magnetic field, Rabi oscillation and Ramsey experiment will be studied.

2.2.1 Microwave Control on NV Centers

Microwave(MW) can be applied as a control of the NV center. This section shows how the transitions between $m_s = 0$ and $m_s = \pm 1$ states are controlled by microwave. The Hamiltonian of a microwave is:

$$H_{contr} = \Omega \cos(\omega_r t + \phi) S_x, \quad (2.13)$$

where Ω is the amplitude of the microwave, ω_r and ϕ are the frequency and phase of the microwave.

The total NV Hamiltonian is:

$$H_{NV} = \Delta S_z^2 + \gamma_e B_z S_z + \Omega \cos(\omega_r t + \phi) S_x. \quad (2.14)$$

At zero magnetic field, the $m_s = +1$ and $m_s = -1$ states are degenerate. Starting from $m_s = 0$, the linearly polarized microwave can not select which state the system evolves to. Instead it will make the $m_s = 0$ state evolve to the superposition of $m_s = \pm 1$ states.

In the rotating frame of H_{rot} ,

$$H_{eff} = e^{iH_{rot}t} (H_{NV} - H_{rot}) e^{-iH_{rot}t}. \quad (2.15)$$

where $H_{rot} = \omega_r S_z^2$ when $\Delta > \omega_z$. Here, $\omega_z = \gamma_e B_z$ is the Zeeman frequency of the NV center.

$$\begin{aligned} H_{eff} &= (\Delta - \omega_r) S_z^2 + \omega_z S_z + e^{i\omega_r t S_z^2} (\Omega \cos(\omega_r t + \phi) S_x) e^{-i\omega_r t S_z^2} \\ &= (\Delta - \omega_r) S_z^2 + \omega_z S_z + \frac{\Omega}{2\sqrt{2}} \begin{pmatrix} 0 & e^{i(2\omega_r t + \phi)} + e^{-i\phi} & 0 \\ e^{-i(2\omega_r t + \phi)} + e^{i\phi} & 0 & e^{-i(2\omega_r t + \phi)} + e^{i\phi} \\ 0 & e^{i(2\omega_r t + \phi)} + e^{-i\phi} & 0 \end{pmatrix} \end{aligned} \quad (2.16)$$

where the time average of the fast rotating terms $e^{-i(2\omega_r t + \phi)}$ and $e^{i(2\omega_r t + \phi)}$ are zero and can be neglected. So

$$\begin{aligned}
H_{eff} &= (\Delta - \omega_r)S_z^2 + \omega_z S_z + \frac{\Omega}{2\sqrt{2}} \begin{pmatrix} 0 & e^{-i\phi} & 0 \\ e^{i\phi} & 0 & e^{i\phi} \\ 0 & e^{-i\phi} & 0 \end{pmatrix} \\
&= (\Delta - \omega_r)S_z^2 + \omega_z S_z + \frac{\Omega}{2} (\cos(\phi)S_x + \sin(\phi)S'_y). \\
&= \begin{pmatrix} \Delta - \omega_r + \omega_z & \frac{\Omega}{2\sqrt{2}}e^{-i\phi} & 0 \\ \frac{\Omega}{2\sqrt{2}}e^{i\phi} & 0 & \frac{\Omega}{2\sqrt{2}}e^{i\phi} \\ 0 & \frac{\Omega}{2\sqrt{2}}e^{-i\phi} & \Delta - \omega_r - \omega_z \end{pmatrix}
\end{aligned} \tag{2.17}$$

where $S'_y = \begin{pmatrix} 0 & i & 0 \\ -i & 0 & -i \\ 0 & i & 0 \end{pmatrix}$. This approximation is called rotating wave approximation(RWA)[46].

Take $|m_s = 0\rangle$ and $|m_s = +1\rangle$ as the two states of a quantum bit for example. In general cases, the microwave frequency is close to the resonant frequency between $|m_s = 0\rangle$ and $|m_s = +1\rangle$:

$$\omega_r \sim \Delta + \omega_z \Rightarrow |\Delta + \omega_z - \omega_r| \lesssim \Omega \tag{2.18}$$

and

$$|\Delta - \omega_z - \omega_r| \sim 2\omega_z \quad \text{when } \omega_z < \Delta \tag{2.19}$$

The microwave amplitude Ω is usually 1-100 MHz while ω_z and Δ is on the order of GHz. Therefore, $\Omega \ll \min(\omega_z, \Delta)$. Let $\delta = \Delta + \omega_z - \omega_r$.

In the resonant case where $\delta = 0$, when there is no external magnetic field $\omega_z = 0$,

$$H_{eff} = \frac{\Omega}{2\sqrt{2}} \begin{pmatrix} 0 & e^{-i\phi} & 0 \\ e^{i\phi} & 0 & e^{i\phi} \\ 0 & e^{-i\phi} & 0 \end{pmatrix} \tag{2.20}$$

The initial state $|m_s = 0\rangle$ will evolve to the superposition of $|m_s = \pm\rangle$ under this Hamiltonian.

When there is a high magnetic field $\omega_z \neq 0$,

$$\begin{aligned}
H_{eff} &= \frac{\Omega}{2\sqrt{2}} \begin{pmatrix} 0 & e^{-i\phi} & 0 \\ e^{i\phi} & 0 & e^{i\phi} \\ 0 & e^{-i\phi} & -2\omega_z \end{pmatrix} \\
&\approx \frac{\Omega}{2\sqrt{2}} \begin{pmatrix} 0 & e^{-i\phi} & 0 \\ e^{i\phi} & 0 & 0 \\ 0 & 0 & -2\omega_z \end{pmatrix}
\end{aligned} \tag{2.21}$$

In the off-resonance case where $\delta \neq 0$,

$$\begin{aligned}
H_{eff} &= \frac{\Omega}{2\sqrt{2}} \begin{pmatrix} \delta & e^{-i\phi} & 0 \\ e^{i\phi} & 0 & e^{i\phi} \\ 0 & e^{-i\phi} & -2\omega_z \end{pmatrix} \\
&\approx \frac{\Omega}{2\sqrt{2}} \begin{pmatrix} \delta & e^{-i\phi} & 0 \\ e^{i\phi} & 0 & 0 \\ 0 & 0 & -2\omega_z \end{pmatrix}
\end{aligned} \tag{2.22}$$

Thus the transition between $|m_s = 0\rangle$ and $|m_s = 1\rangle$ can be realized by this control Hamiltonian. General simple quantum gates can be achieved on NV centers by adjusting the parameters Ω , ϕ , δ and evolving time τ . This is the basic for the ODMR methods introduced in the following sections.

2.2.2 Continuous Wave ODMR

In the continuous-wave(CW) experiment, MW sweeping along a certain frequency range is applied on the NV center. When the MW frequency matches the energy splitting between $|m_s = 0\rangle$ state and $|m_s = +1\rangle$ (or $|m_s = -1\rangle$) state, a resonance absorbing peak can be observed in the spectrum. The CW spectrum can be used to study energy structures of the measured samples.

To perform a continuous wave experiment, a microwave at varying frequencies and a 532 nm laser at a constant power are applied to the NV center. The intensity of the emitted 635 nm red fluorescence against the microwave frequency is measured. The 532 nm laser continuously polarizes the NV electron spins to the $|m_s = 0\rangle$ ground state. If the microwave is off-resonant with the energy splitting between $|m_s = 0\rangle$ and $|m_s = -1\rangle$ or $|m_s = +1\rangle$, the laser will take population at $|m_s = 0\rangle$ to $|m_s = 0\rangle$ in the first excited state and strong fluorescence can be observed when the population goes back to $|m_s = 0\rangle$ in the ground state. At resonant frequency, part of the population at $|m_s = 0\rangle$ is driven to $|m_s = \pm 1\rangle$ states. When the 532 nm laser polarizes the population at $|m_s = \pm 1\rangle$ to $|m_s = 0\rangle$, less fluorescence will be observed due to different relaxation processes taken. So in the CW spectrum, peaks will be seen at every resonant frequency.

CW ODMR can also be used to measure the interaction strength between the NV center and nearby electrons or nuclei. The information about the interaction strength is also shown as peaks in the spectrum as shown in Figure 2.3.

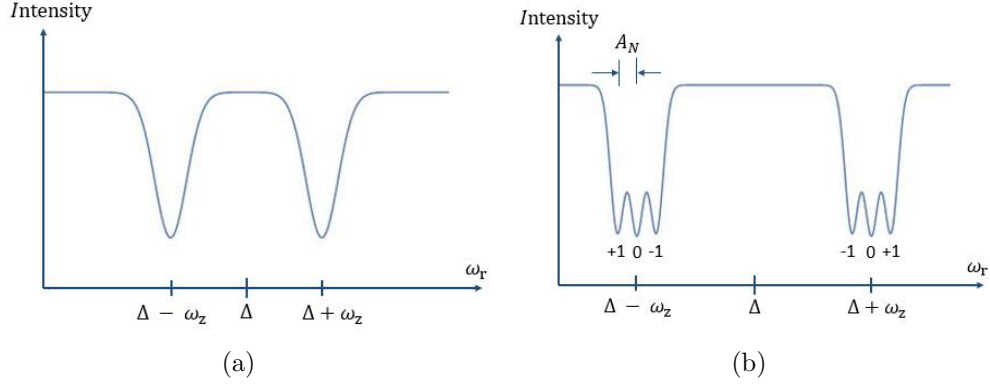


Figure 2.3: (a) and (b) are the simulated CW spectrum without and with NV- ^{14}N hyperfine interaction, respectively.

2.2.3 Pulsed ODMR

While CW experiments provide a method to characterize NV centers, pulsed ODMR is more useful for quantum information processing. The Ramsey experiment and Rabi experiment are two of the commonly used pulsed ODMR experiments on NV centers.

Rabi Experiment

In an applied magnetic field, the transition between $|m_s = 0\rangle$ and $|m_s = +1\rangle$ or $|m_s = -1\rangle$ can be driven with a resonant microwave which generates the population oscillation between the two states. This oscillation, called Rabi oscillation, proves that NV center can be coherently manipulated.

The Rabi oscillation can be measured as follows. Equation 2.21 shows that in the resonant case $\delta = \Delta + \omega_z - \omega_r = 0$, the microwave can generate a transition between $|m_s = 0\rangle$ and $|m_s = +1\rangle$. This resonant microwave lasts for a time duration t_p and then the population at $|m_s = 0\rangle$ is measured. Repeat this for different t_p , and plot the detected photon number vs t_p . The oscillation observed in the plot is the Rabi oscillation. Figure 2.4 illustrates a typical Rabi oscillation experiment, including the needed pulses, results and analysis.

If an nearby ^{14}N is taken into consideration, the Hamiltonian can be written as:

$$H = \Delta S_z^2 + \omega_z S_z + H_{HF}^{14N} + \Omega \cos(\omega_r t + \phi) S_x, \quad (2.23)$$

where $H_{HF}^{14N} = m_I A_N S_z$ is the hyperfine interaction between the NV spin and the ^{14}N nuclear spin, $m_I = 0, \pm 1$ is the spin number of the ^{14}N ; A_N is the hyperfine interaction

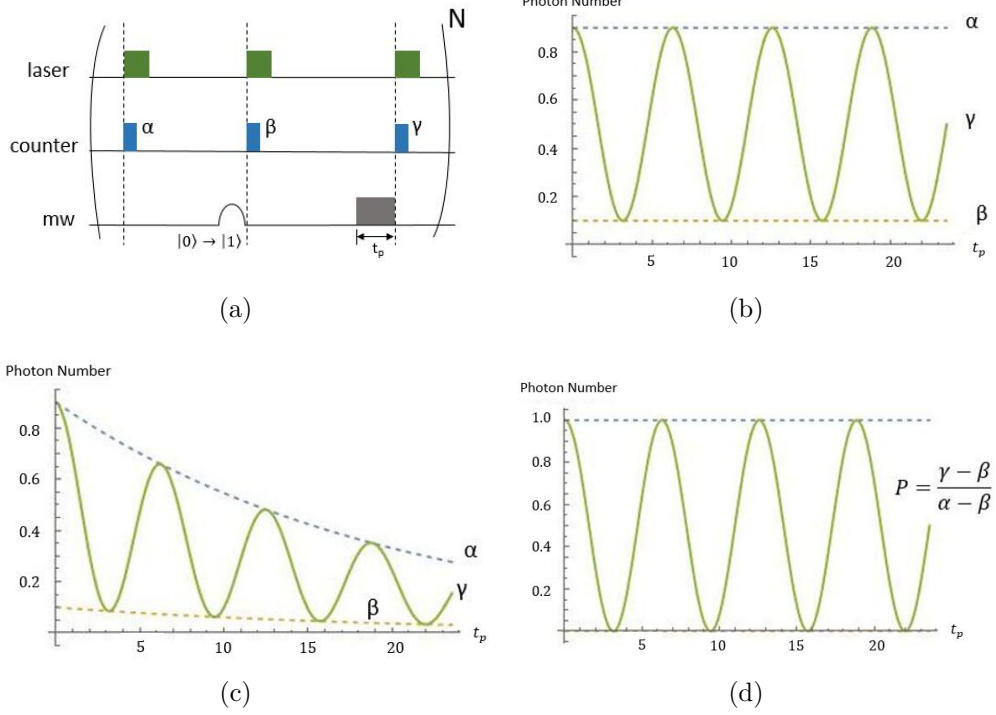


Figure 2.4: (a) shows the single quantum Rabi experiment pulse sequences. α , β and γ are the detected photon numbers by the three laser pulses, respectively. (b) shows the photon numbers measured in (a) vs t_p in the ideal case where $T_2 = \infty$. (c) shows the photon numbers vs t_p with finite T_2 . (d) is the normalized plot of (c) with $P = (\gamma - \beta)/(\alpha - \beta)$ vs t_p . The Rabi oscillation can be seen from (b)-(d). The oscillation frequency is called Rabi frequency.

strength; I_z is the z-component of ^{14}N nuclear spin operator.

In the rotating frame of $\omega_r S_z^2$,

$$\tilde{H} = (\Delta - \omega_r)S_z^2 + \omega_z S_z + m_I A_N S_z + \frac{\Omega}{2} (\cos \phi S_x + \sin \phi S'_y), \quad (2.24)$$

When $\omega_r = \Delta + \omega_z$,

$$\tilde{H} = \begin{pmatrix} m_I A_N & \frac{\Omega}{2\sqrt{2}} e^{-i\phi} & 0 \\ \frac{\Omega}{2\sqrt{2}} e^{i\phi} & 0 & \frac{\Omega}{2\sqrt{2}} e^{i\phi} \\ 0 & \frac{\Omega}{2\sqrt{2}} e^{-i\phi} & 2\omega_z + m_I A_N \end{pmatrix}, \quad (2.25)$$

In the limit of $2\omega_z \gg \Omega$, this Hamiltonian effectively generate an transition between $m_s = 0$

and $m_s = +1$ states while transition between $m_s = 0$ and $m_s = -1$ can be neglected. The Rabi frequencies are different for different m_I . When $m_I = 0$, the Rabi frequency is $\frac{\Omega}{2\sqrt{2}}$. When $m_I = \pm 1$, the Rabi frequency is $\sqrt{\left(\frac{\Omega}{2\sqrt{2}}\right)^2 + (m_I A_N)^2}$. As shown in Figure 2.5(a), the plot of the detected photon number vs t_p consists of three different oscillations where $m_I = 0, \pm 1$ respectively. Figure 2.5(b) is the Fourier transform of the oscillations to analyze their Rabi frequencies.

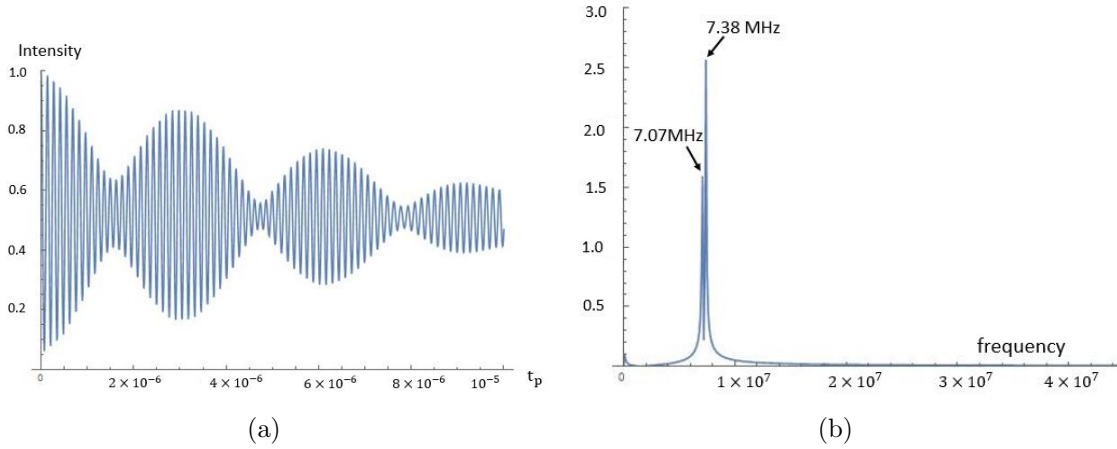


Figure 2.5: (a) is the simulated Rabi experiment at $\Omega = 14$ MHz, $\omega_z = 50$ MHz, in presence of a ^{14}N nuclear spin. (b) is the Fourier transform of (a). It is seen in (b) that there are two peaks at frequencies 7.07 MHz and 7.37 MHz respectively corresponding to the Rabi frequencies when $m_I = 0$ and $m_I = \pm 1$.

Ramsey Experiment

Compared with Rabi experiment in which the driven spin dynamics is observed, a Ramsey experiment can help study the internal spin dynamics. It is also a method for sensing the magnetic field along NV z -axis.

As shown in Figure 2.6, in the Ramsey experiment, following the laser initiation is a $\frac{\pi}{2}$ -pulse around x -axis which takes the initial state $\psi_0 = |m_s = 0\rangle$ to $\psi_1 = (|m_s = 0\rangle + |m_s = -1\rangle)/\sqrt{2}$. After evolving under the Hamiltonian $H_0 = \gamma_e B_z S_z$ for time τ , the system evolves to $\psi_2 = (|m_s = 0\rangle + e^{+i\gamma_e B_z \tau} |m_s = -1\rangle)/\sqrt{2}$ and another $\frac{\pi}{2}$ -pulse is applied for detection. The final state is $\psi_3 = \cos(\gamma_e B_z \tau) |m_s = 0\rangle + i \sin(\gamma_e B_z \tau) |m_s = -1\rangle$. The

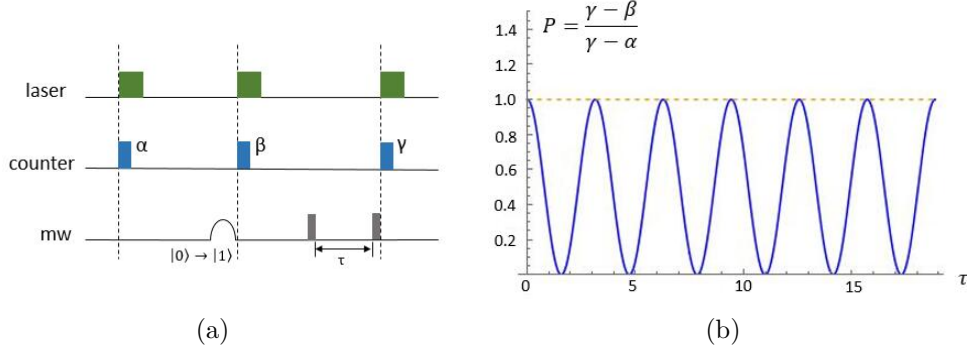


Figure 2.6: (a) shows the pulse sequence for Ramsey experiment. α , β and γ are the detected photon numbers. Counts α and β provide the comparison for the real Ramsey experiment count γ . (b) is the plot $P = (\gamma - \beta)/(\alpha - \beta)$ vs τ .

detected $|m_s = 0\rangle$ intensity as a function of τ is $I = \cos^2(\gamma_e B_z \tau)$. Plot the detected intensity vs τ , the z-direction magnetic field B_z can be calculated from the oscillation frequency ω_B : $B_z = \frac{2\omega_B}{\gamma_e}$.

2.3 Confocal Microscope

Confocal microscopes are used to investigate only one NV center at one time in the bulk diamonds which contain many NV centers. Figure 2.7 shows the simplified model of the confocal microscope. Optic signals at points $S_{\{1,2,3,4\}}$ will form images at their conjugate points $S'_{\{1,2,3,4\}}$, respectively. However, a pinhole at S'_1 will block all the other light and only allow the light from S_1 to pass. The pinhole needs to be placed to meet this requirement and in this way the pinhole and the point light source of interest, S_1 , can be said to fulfill the confocal condition.

A scanning confocal microscope is needed to detect more than one point light source, which is necessary for finding NV centers in a bulk diamond sample. The sample diamond with NV centers can be moved and different point sources are taken to the confocal point. In practical experiment setup as shown in Figure 2.8, the scanning confocal microscope consists of several parts: source, switch arm, mode shaping arm, scanning optics and detecting part.

Switch Arm

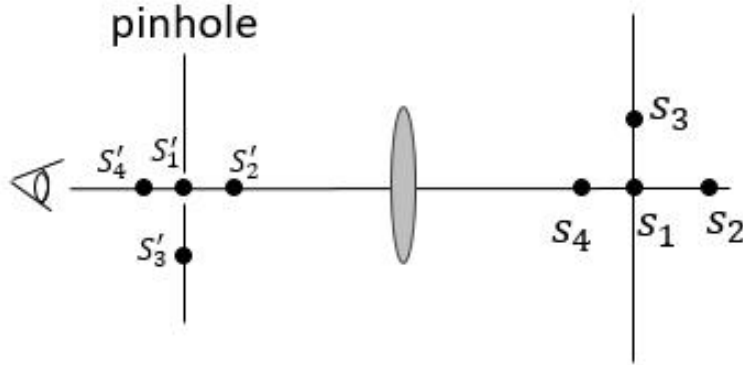


Figure 2.7: The simplified model of the confocal microscope. Only the optic signal at S_1 can be detected in presence of the pinhole.

ODMR experiments with NV centers requires the laser to be on and off with fast switching time. Instead of an expensive laser apparatus, a switching arm with an acousto-optic-modulator (AOM) is used, which allows a switching time on the order of 10 ns.

AOM can diffract light using sound wave. When the piezoelectric material in AOM is driven, the optical medium will oscillate mechanically, causing its refraction index to change. The changed refraction index results in Bragg diffraction on the laser passing through. The diffraction angle is:

$$\theta_{bragg} = \arcsin\left(\frac{n\lambda}{2d}\right), \quad (2.26)$$

where n is the diffraction order.

The first order diffraction is picked for experiment by an iris. When the AOM is off, there is only zeroth order, so the laser is blocked. When the AOM is on, the first order light passes through.

A switching arm consists of AOM, polarized beam splitter(PBS), $\frac{\lambda}{4}$ -wave plate (QWP), $\frac{\lambda}{2}$ -wave plate (HWP), lenses and mirrors. The input p-polarized laser is transmitted through the PBS into the AOM. After the AOM, a QWP rotate the p-polarized laser to a circularly polarized laser. After the laser is reflected by the mirror a QWP will rotate the laser to an s-polarized laser, which will be reflected by the PBS into the next section.

Mode Shaping Arm

Following the switching arm, a mode-shaping arm is used to correct the spatial mode aberrations of the input laser with a single mode fiber. The output laser from the mode shaping arm is reflected by a dichroic mirror to the scanning optics. A dichroic mirror reflects laser at 532 nm wavelength and allows laser with 550-825 nm wavelength to pass. So the output 635 nm red light from the scanning optics can transmit to the detecting part.

Scanning Optics

The scanning optics consists of a galvanometers(galvos) with scanning mirrors, a scanning telescope and the objective. To have a high resolution of around $1 \mu m^2$, an objective is used instead of a lens. An objective needs the input light to be collimated, so another lens is needed in front of the objective. A galvanometer is composed of two mirrors with 45° between them. We can adjust the mirrors to control the scanning laser. Two lenses placed in front of the objective are used as the scanning telescope. The distance between the two lenses should be the sum of the two lenses' focal lengths. A scanning telescope enlarges the radius of the laser beam and fulfill the objective to have enough light shining on the NV centers.

With this setup, we are able to read out the states of different NV centers separately in the experiments.

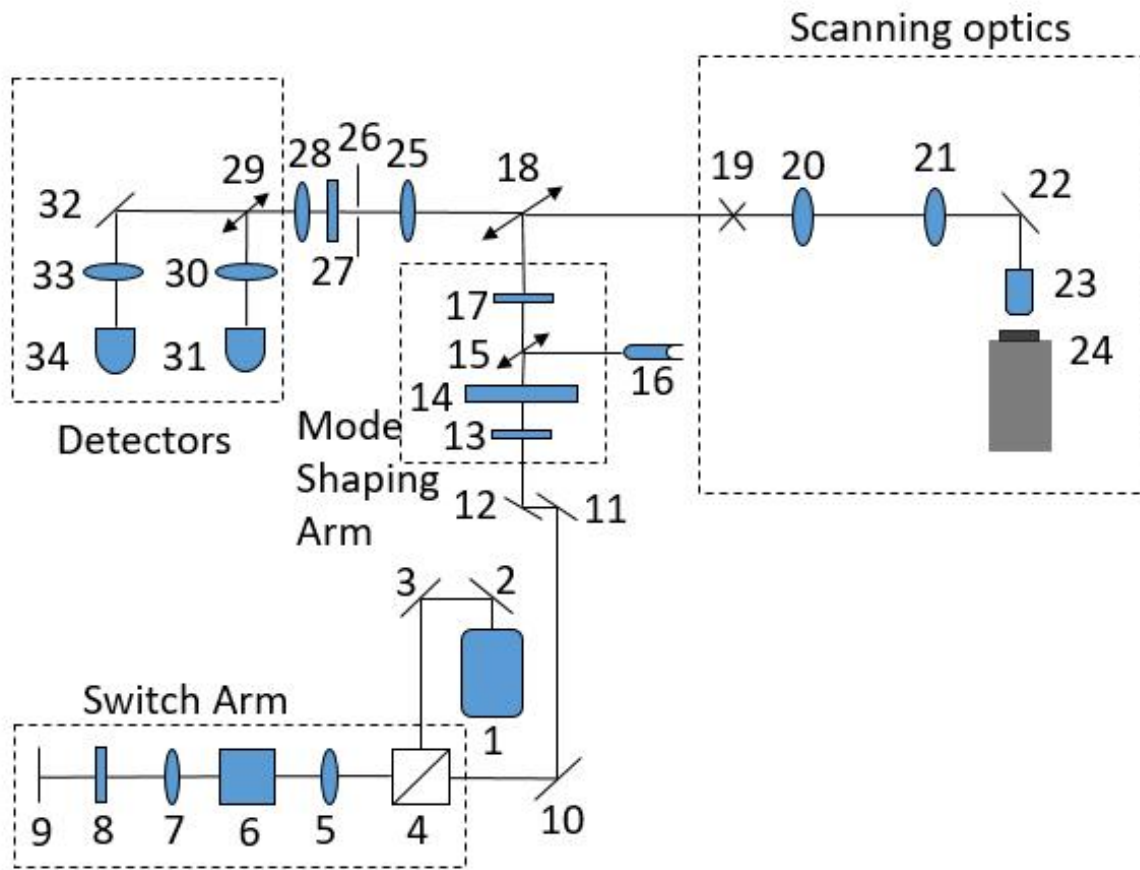


Figure 2.8: The practical confocal microscopy design. The part names are listed in Table 2.1.

No.	Name	No.	Name
1	Laser	18	Dichroic Mirror
2	Mirror	19	Galvos
3	Mirror	20	Lens
4	Polarizing Beam Splitter	21	Lens
5	Lens	22	Mirror
6	AOM	23	Object
7	Lens	24	Sample and sample stage
8	$\lambda/4@532$ nm	25	Lens
9	Mirror	26	100 μm Pinhole
10	Mirror	27	Longpass filter
11	Mirror	28	Lens
12	Mirror	29	Pellicle Mirror
13	Continuously variable NVD filter	30	Lens
14	Neutral Density Filters	31	Single Photon Counting
15	Pellicle Mirror	32	Mirror
16	Power Meter	33	Lens
17	$\lambda/2@532$ nm	34	Single Photon Counting

Table 2.1: The list of names corresponding to the part numbers labeled in Figure 2.8.

Chapter 3

NV centers as a Magnetic Sensor of Spin

A good magnetic sensor requires stability, a method to read out, high sensitivity to study small magnetic field at room temperature and a relatively small size to achieve spatial resolution. NV centers have a long coherence time with optical and magnetic properties, which makes it a valuable nano-scale magnetic sensor.

NV center can be a sensor of magnetism based on the Zeeman splitting[23] caused by external magnetic field along z-axis, which will break the degeneracy of $m_s = \pm 1$ states. The separation between $m_s = -1$ and $m_s = +1$ states is proportional to the external magnetic field seen by the NV center which can be measured by the CW spectrum on NV. The magnetic field along z-axis of the NV center can also be measured by Ramsey-type measurement with better accuracy because it eliminates environment noise.

NV centers can also sense spins based on the dipole-dipole interaction between NV centers and the spins. The position of a single spin, the density of a spin ensemble and the interaction network among the spin ensemble are possible properties that can be studied by NV centers. In the first part of this chapter, the dipole-dipole interaction and its secular approximation will be introduced; in the second part, a theoretic method to determine the position of an electron spin with several NV centers and the simulation results will be presented.

3.1 Dipole-dipole Interaction and Secular Approximation

3.1.1 Introduction to Dipole-dipole Interaction

The direct interaction between two magnetic moments are called dipole-dipole interaction. In the case of spin physics, if the spin operators of the two spins are \vec{S}_1 and \vec{S}_2 and separated by a distance $|\vec{r}'|$, the dipole-dipole interaction between these two spins is:

$$H_{dip} = \frac{\mu_0 \gamma_1 \gamma_2}{4\pi |\vec{r}'|^3} \left(3 \left(\vec{S}_1 \cdot \hat{r} \right) \left(\vec{S}_2 \cdot \hat{r} \right) - \vec{S}_1 \cdot \vec{S}_2 \right) \quad (3.1)$$

where μ_0 is the vacuum permeability, γ_1 and γ_2 are the gyromagnetic ratios of the two spins; $\vec{r}' = |\vec{r}'| \hat{r}$ is the vector pointing from the first spin to the second spin or reverse and \hat{r} is its unit vector.

This dipole-dipole Hamiltonian can be decomposed to six components[46] according to how each component affects the states of the system:

$$H_{dip} = \frac{\mu_0 \gamma_1 \gamma_2}{4\pi |\vec{r}'|^3} (A + B + C + D + E + F) \quad (3.2)$$

where

$$\begin{aligned} A &= S_z^1 S_z^2 (1 - 3 \cos^2 \theta), \\ B &= -0.25(S_+^1 S_-^2 + S_-^1 S_+^2)(1 - 3 \cos^2 \theta), \\ C &= -1.5(S_+^1 S_z^2 + S_z^1 S_+^2) \sin \theta \cos \theta e^{-i\phi}, \\ D &= -1.5(S_-^1 S_z^2 + S_z^1 S_-^2) \sin \theta \cos \theta e^{+i\phi}, \\ E &= -0.75 S_+^1 S_+^2 \sin^2 \theta e^{-2i\phi}, \\ F &= -0.75 S_-^1 S_-^2 \sin^2 \theta e^{+2i\phi}. \end{aligned} \quad (3.3)$$

Here θ and ϕ are the polar coordinates of the vector $\vec{r}' = |\vec{r}'| \hat{r}$, $S_+ = S_x + iS_y$ and $S_- = S_x - iS_y$ can raise or lower the energy level of a given state.

3.1.2 Dipole-dipole Interaction under Secular Approximation

The dipole-dipole interaction Hamiltonian can be simplified by secular approximation when a large magnetic field is present.

Assuming $H = H_0 + H_1$ where H_0 is the dominant term. In the perturbing Hamiltonian H_1 , the parts that commute with H_0 are usually called secular terms, H_{sec} . In the rotating frame of H_0 :

$$\begin{aligned}\tilde{H} &= e^{-iH_0t}(H - H_0)e^{iH_0t} \\ &= e^{-iH_0t}(H_{sec} + H'_1)e^{iH_0t} \\ &= H_{sec} + e^{-iH_0t}H'_1e^{iH_0t}\end{aligned}\quad (3.4)$$

where $H'_1 = H - H_{sec}$ is the part that does not commute with H_0 . $\tilde{H}'_1 = e^{-iH_0t}H'_1e^{iH_0t}$ is time-dependent and averages to 0 when the evolving time T is long:

$$\lim_{T \rightarrow \infty} \int_0^T \tilde{H}'_1 dt = 0. \quad (3.5)$$

So the secular terms are kept while the non-secular terms are neglected in the secular approximation.

Electron-electron dipolar interaction

At zero field, there is no spatial preference in the system so all the terms in the dipolar Hamiltonian stays.

$$H_{dip} = \frac{\mu_0 \gamma_e^2}{4\pi |\vec{r}|^3} (3(\vec{\sigma} \cdot \hat{r})(\vec{\sigma} \cdot \hat{r}) - \vec{\sigma} \cdot \vec{\sigma}). \quad (3.6)$$

If there is a high magnetic field B_0 along z-axis, $H_0 = \gamma B_0 \sigma_z^1 + \gamma B_0 \sigma_z^2$.

$$\begin{aligned}\lim_{T \rightarrow \infty} \int_0^T e^{-iH_0t} J e^{iH_0t} dt &\neq 0, (J = A, B) \\ \lim_{T \rightarrow \infty} \int_0^T e^{-iH_0t} K e^{iH_0t} dt &= 0. (K = C, D, E, F).\end{aligned}\quad (3.7)$$

So in the presence of a strong external magnetic field, the approximated dipolar Hamiltonian is

$$H_{dip} = \frac{\mu_0 \gamma_e^2}{4\pi |\vec{r}|^3} (3\sigma_z \sigma_z - \vec{\sigma} \cdot \vec{\sigma})(1 - 3\cos^2 \theta), \quad (3.8)$$

NV-electron dipolar interaction

At zero magnetic field, the zero field splitting term is the dominant term ΔS_z^2 . The dipole-dipole Hamiltonian, the secular terms and the non-secular terms are listed as follows:

$$H_{dip} = \frac{\mu_0 \gamma_e^2}{4\pi |\vec{r}|^3} \left(3 \left(\vec{S} \cdot \hat{r} \right) \left(\vec{\sigma} \cdot \hat{r} \right) - \vec{S} \cdot \vec{\sigma} \right), \quad (3.9)$$

$$\begin{aligned}\lim_{T \rightarrow \infty} \int_0^T e^{-i\Delta S_z^2 t} J e^{i\Delta S_z^2 t} dt &\neq 0, (J = A, C, D) \\ \lim_{T \rightarrow \infty} \int_0^T e^{-i\Delta S_z^2 t} K e^{i\Delta S_z^2 t} dt &= 0. (K = B, E, F)\end{aligned}\quad (3.10)$$

So when there is no external magnetic field, the approximated dipolar Hamiltonian is

$$H_{dip} = \frac{\mu_0 \gamma_e^2}{4\pi |\vec{r}|^3} [S_z \sigma_z (1 - 3 \cos^2 \theta) - 3(S_x \sigma_z + S_z \sigma_x) \sin \theta \cos \theta] \quad (3.11)$$

with $\phi = 0$.

If there is a high magnetic field B_0 along z-axis, the dominant terms are $H_0 = \gamma B_0 \sigma_z$. We can get the secular and non-secular terms:

$$\begin{aligned}\lim_{T \rightarrow \infty} \int_0^T e^{-iH_0 t} J e^{iH_0 t} dt &\neq 0, (J = A) \\ \lim_{T \rightarrow \infty} \int_0^T e^{-iH_0 t} K e^{iH_0 t} dt &= 0, (K = B, C, D, E, F)\end{aligned}\quad (3.12)$$

So in the presence of a strong external magnetic field, the approximated dipolar Hamiltonian is

$$H_{dip} = \frac{\mu_0 \gamma_e^2}{4\pi |\vec{r}|^3} S_z \sigma_z (1 - 3 \cos^2 \theta). \quad (3.13)$$

NV-NV dipolar interaction

In zero field, the zero field splitting term is the dominant terms $\Delta(S_z^2 \otimes \mathbb{1} + \mathbb{1} \otimes S_z^2)$. The dipolar Hamiltonian and the secular and non-secular terms can be expressed as:

$$H_{dip} = \frac{\mu_0 \gamma_1 \gamma_2}{4\pi |\vec{r}|^3} \left(3 \left(\vec{S} \cdot \hat{r} \right) \left(\vec{S}' \cdot \hat{r} \right) - \vec{S} \cdot \vec{S}' \right), \quad (3.14)$$

$$\begin{aligned}\lim_{T \rightarrow \infty} \int_0^T e^{-i\Delta S_z^2 t} J e^{i\Delta S_z^2 t} dt &\neq 0, (J = A, B, E, F) \\ \lim_{T \rightarrow \infty} \int_0^T e^{-i\Delta S_z^2 t} K e^{i\Delta S_z^2 t} dt &= 0. (K = C, D)\end{aligned}\quad (3.15)$$

Therefore, when there is no external magnetic field, the approximated dipolar Hamiltonian is

$$H_{dip} = \frac{\mu_0 \gamma_e^2}{4\pi |\vec{r}|^3} \left[\left(S_z S_z - \frac{i}{2} (S_y S_x - S_x S_y) \right) (1 - 3 \cos^2 \theta) - \frac{3}{4} \sin^2 \theta (S_+ S_+ e^{-2i\phi} + S_- S_- e^{2i\phi}) \right]. \quad (3.16)$$

If there is a high magnetic field B_0 along z-axis, the dominant terms are $\gamma_e B_0(S_z \otimes \mathbb{1} + \mathbb{1} \otimes S_z) + \Delta(S_z^2 \otimes \mathbb{1} + \mathbb{1} \otimes S_z^2)$, and thus the secular and non-secular terms are

$$\begin{aligned} \lim_{T \rightarrow \infty} \int_0^T e^{-iH_0 t} J e^{iH_0 t} dt &\neq 0, (J = A, B) \\ \lim_{T \rightarrow \infty} \int_0^T e^{-iH_0 t} K e^{iH_0 t} dt &= 0. (K = C, D, E, F) \end{aligned} \quad (3.17)$$

So in the presence of a strong external magnetic field, the approximated dipolar Hamiltonian is

$$H_{dip} = \frac{\mu_0 \gamma_e^2}{4\pi |\vec{r}|^3} (3S_z S_z - \vec{S} \cdot \vec{S}) (1 - 3\cos^2 \theta) \quad (3.18)$$

which has the same form as Eq.3.8.

3.2 Locating an Electron Spin with Two NV centers

As introduced in the above section, the strength of the dipole-dipole interaction between two spins depends on their relative positions and spin orientations. Therefore, with multiple NV centers interacting with a target spin, it is possible to get the accurate position information of the target spin from the NV centers.

There is an example of locating a single electron spin in a sample material by using two nearby NV centers, and simulations were done to estimate the sensing ability of the two NV centers. The machine learning method[43][44] is used as the learning algorithm. The criteria for the sensing ability is the Fisher information which indicates the amount of information that the observable carries about an unknown parameter[39][40][42]. In this case, the observable is the ODMR signals collected from NV centers and the unknown parameter is the position of the target spin. The more information the observable carries, the more accurate the target position can be.

A machine learning Python program written by Chris Ferrie, Christopher Granade, Ian Hincks, etc. is used for simulations in the following demonstration.

3.2.1 Estimating the Locating Ability

As shown in Figure 3.1, two NV centers separated by 10 nm in the diamond are used to locate a single electron spin in the sample. The Hamiltonian of this system can be written

as:

$$H = H_{ZFS} + H_{Zeeman} + H_{dip}, \quad (3.19)$$

where the dipole-dipole interaction H_{dip} includes $NV - e^-$ and $NV - NV$ interactions:

$$H_{dip} = H_{NV-NV} + H_{NV-e^-}^1 + H_{NV-e^-}^2, \quad (3.20)$$

To collect the location information of the target spin from NV centers, a Ramsey experiment is done simultaneously on both NV centers. Figure 3.1(b) shows the Fisher information for every possible position of the target spin. The brighter a position is, the larger the Fisher information of this position is, and the more accurately it is able to tell whether the spin is at this position. The two bright spots are the two NV centers. The dark curve line between the two NV centers shows that it is harder to locate a spin on this curve than in other brighter areas. This difficulty of locating on the curve results from the symmetry of this two-NV system. To break this symmetry and have a better imaging ability for all the spots in the area, a relative movement is performed between the sample and the diamond. Combining the results from before and after the movement, the possibility that the target spin is at each position can be calculated with the help of maximum likelihood estimation (MLE) [58].

3.2.2 Locating the Target Spin using Maximum Likelihood Estimation

To locate the target spin using MLE, repetitive Ramsey experiments are simulated. For each Ramsey duration t , 500 repetitions are done and a set of simulated data of detected photon counts is obtained. The probability of getting this set of data given that the position of the target spin is at (x, z) can be calculated, named as $P_{(x,z,t)}$. The experiments with 200 different durations are simulated. If we add up the logarithms of those probabilities got from different durations t for each position (x, z) , $Log = \sum_t \log P_{(x,z,t)}$, and plot Log vs (x, z) , it will be easy to see which is the position of the target spin that is the most likely to generate these sets of Ramsey experiment results.

The simulation results are shown in 3.1(c) and (d). It is assumed that the target spin is at (4 nm, 2 nm). As shown in Figure 3.1(c), when the sample and the diamond have no relative movement, the two symmetric points about the line $x=5$ nm, (4 nm, 2 nm) and (6 nm, 2 nm), can not be distinguished. While in Figure 3.1(d), combining the results before and after a movement of 2 nm, it is seen that (4 nm, 2 nm) is the most likely point where the target spin is.

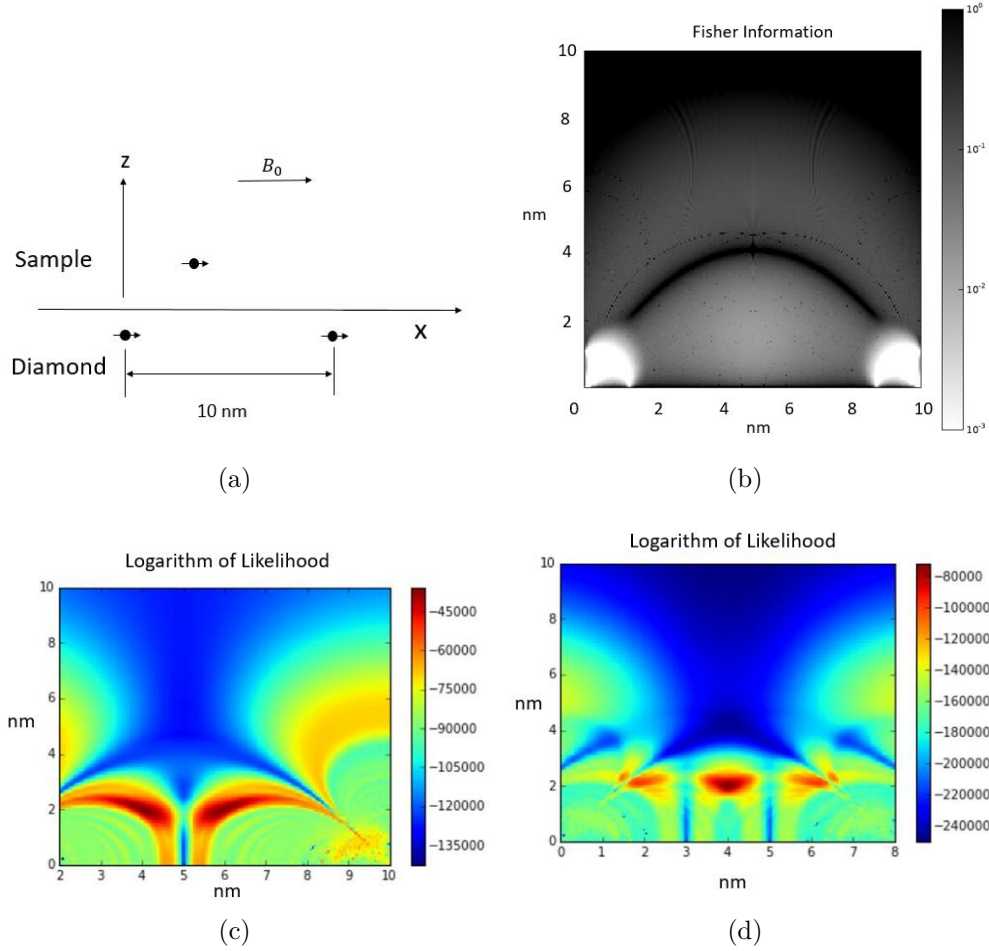


Figure 3.1: (a) Two NV centers in the diamond separated by 10nm are used to detect the spin in the nearby sample film. The axis directions are shown in (a). The NV principle axis and the B_0 magnetic field are along x-axis. (b) The Fisher information for every possible position of the target spin. The gray scale shows the achievable accuracy. The brighter a position is, the larger the Fisher information of this position is, and the more accurate the locating can be. (c) and (d) are the logarithm of the likelihood that the target spin is at each position. In the simulation, it is assumed that the actual spin is positioned at (4,2). In (c), no relative movement is made between the sample and the diamond, and both (4,2) and (6,2) points are the most likely spin locations. In (d) a movement of 2 nm is made and (4,2) is the most likely spin location.

The above simulations prove it possible in theory to locate a single electron spin with a nanometer resolution using two NV centers. However, in practical, it is hard to move the sample material relative to the diamond without breaking them. Choosing more than two NV centers as the sensor can be a solve but locating more than two NV centers accurately is also a challenge. Another problem of this method is that NV centers are not completely static in the crystal. If this fact is taken into consideration in the above simulation, the resulting Fisher information will be much smaller. However, this simulation provides a general view of how NV centers can be used as a magnetic sensor of spins by using the dipole-dipole interaction between NVs and the target spins. With some adjustments to this method, the problems mentioned above are possible to be solved.

Chapter 4

NV Centers with Mechanical Motion as a Sensor of Thin Films

Molecular monolayer films can be fabricated in labs recently. With spin network containing nuclear or electron spins, the thin films act as mesoscopic systems that have increasingly importance in quantum information processing. To be able to use this spin network in the films, it is necessary to measure the interactions among the spins. This chapter proposes a scheme of a thin film sensor with atomic resolution and high sensitivity, which is made of NV centers with mechanical motions. Control pulse sequences needed for this scheme are developed in this chapter and the following chapter.

4.1 Thin Film Sensing with NV centers

With the properties introduced in the previous chapters, NV centers are broadly used as quantum sensors for different parameters. As shown in Figure 4.1, NV centers are usually used to sense a magnetic source by measuring the interaction between the NV center and the target magnetic source. For example, to detect a single electron spin, the dipole-dipole interaction between the NV center and the electron spin is of interest; to determine the strength of a magnetic field, the Zeeman splitting of the NV center is measured, which shows the interaction between the NV center and the field. However, when the target is to characterize a thin film, we are more interested in the strength of the internal interactions among the spin ensemble in the film instead of the NV-spin interactions. The idea is to make the film spins evolve under the internal interactions while the NV-spin interactions

are used to transfer the state information between thin film spins and NV centers, and finally the NV center states that contain the information of the spin network are read out optically. To enhance the sensing sensitivity, the use of NV centers with mechanical motions is proposed and will be demonstrated in this thesis.

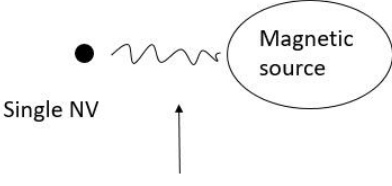
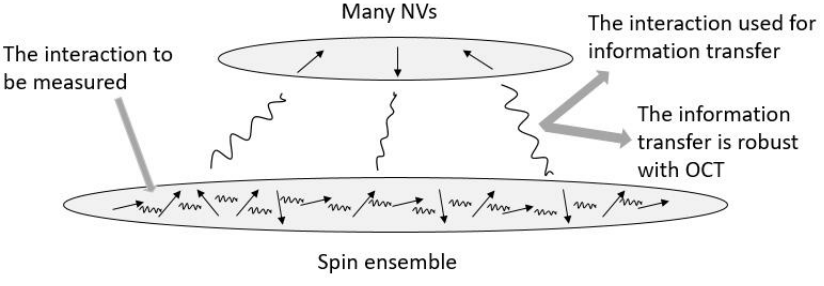
What most people do	The scheme propose here
 <p data-bbox="235 699 332 724">Single NV</p> <p data-bbox="483 625 592 682">Magnetic source</p> <p data-bbox="316 793 560 850">The interaction that people usually measure</p>	 <p data-bbox="998 567 1112 588">Many NVs</p> <p data-bbox="665 609 836 640">The interaction to be measured</p> <p data-bbox="1242 577 1477 630">The interaction used for information transfer</p> <p data-bbox="1291 661 1469 745">The information transfer is robust with OCT</p> <p data-bbox="974 808 1120 829">Spin ensemble</p>
<p data-bbox="227 865 633 972">Use one NV to characterize a magnetic source (eg. single spin).</p>	<p data-bbox="665 865 1485 972">Instead of using one NV to characterize very locally, we use an ensemble of NV centers to measure the average properties of the target thin film.</p>

Table 4.1: An illustration of the difference between how most people use NV as sensors and how this thesis proposes to use NV centers as film sensors.

4.2 Use NV Centers with Motion to Identify Spins in the Thin Film

When the spin interactions in the thin film are to be measured, it is necessary to have these spins evolve under the interactions without being affected by the NV centers. This requires the decoupling of the NV- e^- dipolar interactions during the evolving time. However, to allow the information transfer between the NV centers and the target spins, the NV- e^- interactions are needed while the NV-NV and e^- - e^- interactions need to be decoupled to have better sensitivity. Chapter 5 will introduce the method to decouple the NV- e^- interactions. In the following section, a pulse sequence is demonstrated to decouple the homo-spin dipolar interactions. In this decoupling procedure, the NV- e^- interactions are affected as well. The recoupling of the affected NV- e^- interactions by adding mechanical motions to the NV centers will also be introduced. Optimal control theory is also employed in this design to promote the robustness of the microwave controls on the oscillating NV centers.

The concept model of the spin-mechanical sensor is shown in Figure 4.1. The cantilever is a quartz tuning fork, whose resonant frequency is 32 kHz, which is close to the frequency of the dipolar interactions among the electrons in the sample film. Ideally, the NV centers are attached to one prong of the tuning fork so that the NV sensors can be used to scan the thin film by operating the AFM. However, it is difficult to optically read out the states of moving NV centers. Therefore, the thin film is placed on top of the cantilever instead and the diamond with NV centers is fixed. When the NV centers are nanometers away from the sample film, the dipolar interactions are strong enough to transfer information between NV centers and the film spins.

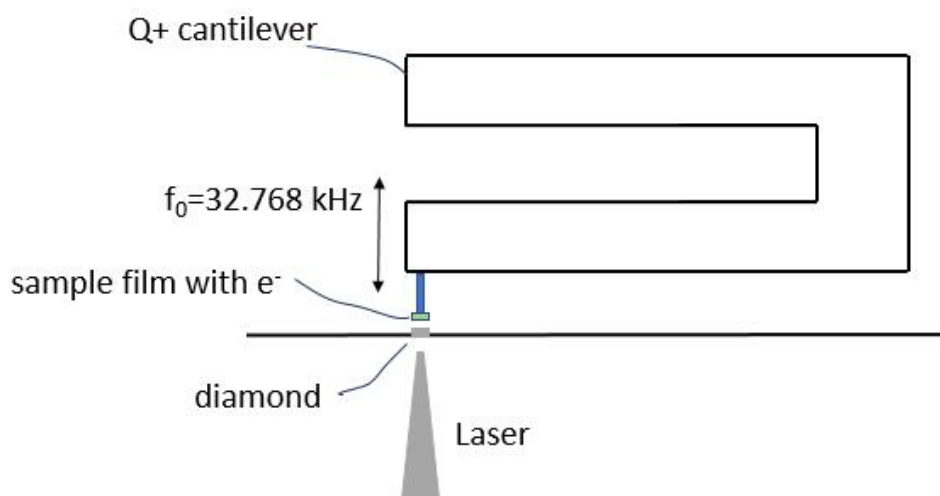


Figure 4.1: The concept model of the thin film sensor. The motion of the sensor is provided by the oscillation of the quartz tuning fork, which is the tip of an AFM. In the ideal case, the NV centers are attached to the tuning fork so that the NV sensors can be used to scan the thin film by operating the AFM. However, it is difficult to optically read out the states of the moving NV centers, so the thin film is placed on top of the cantilever instead and the diamond with NV centers is fixed and detected by lasers.

4.2.1 Homo-spin Dipolar Interaction Decoupling with a 12-pulse Sequence in the Strong Magnetic Field

An important part of the NV thin film sensor is to decouple the homo-spin dipolar interactions during the information transfer process between the NV centers and the e⁻ spin network. A 12-pulse sequence can be used for this decoupling purpose. It should be mentioned here that although a decoupling sequence that works at zero magnetic field is preferred for high sensitivity, we will leave it for future study and first work on this 12-pulse sequence that works at high field. The Average Hamiltonian Theory (AHT) is the basic mathematical method to analyze the effect of the pulse sequence on spin interactions.

Average Hamiltonian Theory(AHT) and Toggling Frame

To understand the AHT, we start with the time-dependent Schrödinger equation:

$$\frac{d}{dt} |\Psi(t)\rangle = -iH(t) |\Psi(t)\rangle, \quad (4.1)$$

where $H(t)$ and $|\Psi(t)\rangle$ are the system Hamiltonian and state at time t . So for an initial state $|\Psi(0)\rangle$, $|\Psi(t)\rangle$ is given by $|\Psi(t)\rangle = U(t) |\Psi(0)\rangle$, where $U(t)$ is a unitary that satisfies,

$$\frac{d}{dt} U(t) = -iH(t)U(t), \quad (4.2)$$

and

$$U(0) = \mathbb{1}. \quad (4.3)$$

Solve for $U(t)$ and expand with the Magnus expansion,

$$\begin{aligned} U(t) &= \mathcal{T} \exp(-i \int_0^t dt' H(t')) \\ &= \exp[-i(\bar{H}^{(0)} + \bar{H}^{(1)} + \bar{H}^{(2)} + \dots)t] \end{aligned} \quad (4.4)$$

where

$$\begin{aligned} \bar{H}^{(0)} &= \frac{1}{t} \int_0^t dt_1 H(t_1), \\ \bar{H}^{(1)} &= \frac{-i}{2t} \int_0^t dt_1 \int_0^{t_1} dt_2 [H(t_1), H(t_2)], \\ \bar{H}^{(2)} &= \frac{-1}{6t} \int_0^t dt_1 \int_0^{t_1} dt_2 \int_0^{t_2} dt_3 ([H(t_1)[H(t_2), H(t_3)] + [H(t_3), [H(t_2), H(t_1)]]), \\ &\dots \end{aligned} \quad (4.5)$$

$\bar{H}^{(n)}$ are the n^{th} -order average Hamiltonian.

Suppose there is a pulse sequence R_1, R_2, \dots, R_n where R_k ($k=1,2,\dots,n$) represent the rotation unitary of each pulse. $\Delta t_1, \Delta t_2, \dots, \Delta t_n$ are the time period between two nearest pulses.

If the initial state is ρ_{in} , its final state ρ_f after this pulse sequence is

$$\begin{aligned}\rho_f &= (U_n R_n U_{n-1} \cdots U_2 R_2 U_1 R_1) \rho_{in} (U_n R_n U_{n-1} \cdots U_2 R_2 U_1 R_1)^\dagger. \\ &= \Lambda \rho_{in} \Lambda^\dagger,\end{aligned}\quad (4.6)$$

where

$$\begin{aligned}\Lambda &= U_n R_n U_{n-1} \cdots U_2 R_2 U_1 R_1 \\ &= (R_n \cdots R_1) (R_n \cdots R_1)^\dagger U_n (R_n \cdots R_1) (R_1^\dagger \cdots R_{n-1}^\dagger) R_n^\dagger R_n U_{n-1} \cdots U_1 R_1 \\ &= (R_n R_{n-1} \cdots R_2 R_1) \tilde{U}_n \tilde{U}_{n-1} \cdots \tilde{U}_1,\end{aligned}\quad (4.7)$$

and $\tilde{U}_k = (R_k \cdots R_1)^\dagger U_k (R_k \cdots R_1)$.

To calculate the corresponding Hamiltonian \tilde{H}_k to the unitary \tilde{U}_k , let $R = R_k \cdots R_1$, and

$$\begin{aligned}R^\dagger \tilde{U} R &= R^\dagger e^{-iHt} R \\ &= R^\dagger \left(\mathbb{1} - iHt + \frac{(-it)^2}{2!} H^2 + \cdots \right) R \\ &= \mathbb{1} - it R^\dagger H R + \frac{(-it)^2}{2!} (R^\dagger H R)^2 + \cdots \\ &= \exp[-it(R^\dagger H R)] = \exp[-it\tilde{H}].\end{aligned}\quad (4.8)$$

So during the k^{th} time interval Δt_k , the effective Hamiltonian, also called the toggling Hamiltonian,

$$\tilde{H}_k = (R_k R_{k-1} \cdots R_1)^\dagger H_0 (R_k R_{k-1} \cdots R_1), \quad (4.9)$$

where H_0 is the spin interaction Hamiltonian in absence of the pulse sequence.

So the average Hamiltonian to its 0^{th} order can be calculated as $\bar{H} = \frac{1}{\sum_k \Delta t_k} \sum_k \tilde{H}_k \Delta t_k$. In this way, if the pulse sequence is well-designed, the spin interaction H_0 can be decoupled in the time duration of the pulse sequence..

12-pulse decoupling sequence

There are different decoupling sequence for electron dipolar interaction. WAHUA[49] and MREV-4[50] are the typical ones. The decoupling sequence that will be used in our experiment is a 12-pulse sequence containing 12 $\pi/2$ pulses about x-axis or y-axis as shown

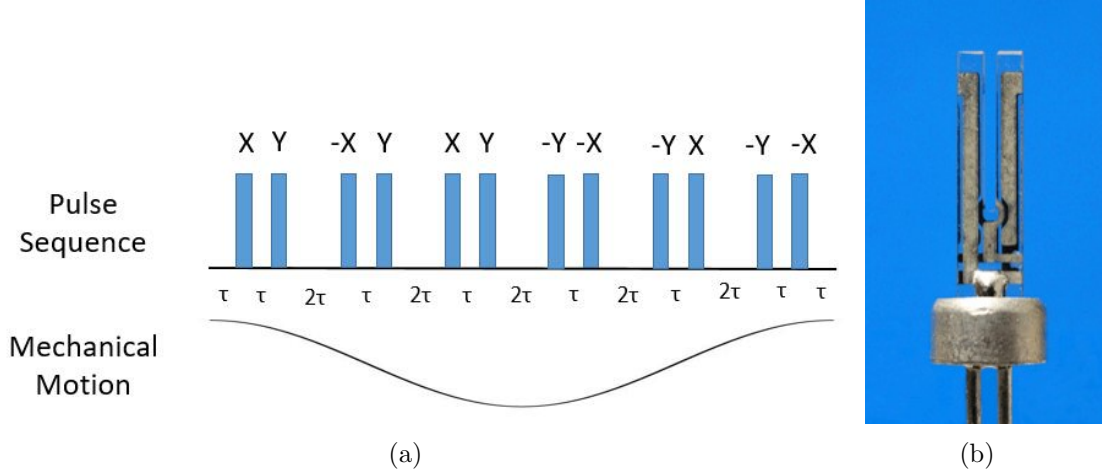


Figure 4.2: (a) The 12-pulse sequence and corresponding mechanical motion of the tuning fork. The period of the mechanical oscillation matches the full time duration of the pulse sequence. (b) A picture of the quartz tuning fork.

in Figure 4.2. According to Chapter 3, in the presence of a strong external magnetic field along z -axis, the dipole-dipole interaction between two electron spins is Eq. 3.8.

Calculate the zeroth order average Hamiltonian using toggling frame:

$$\begin{aligned}
 \bar{H} &= \frac{\mu_0 \gamma_e^2}{4\pi r^3} \frac{1}{18\tau} [3\tau(\sigma_z \sigma_z + \sigma_y \sigma_y + 2\sigma_x \sigma_x + \sigma_z \sigma_z + 2\sigma_y \sigma_y + \sigma_x \sigma_x + 2\sigma_z \sigma_z \\
 &\quad + \sigma_x \sigma_x + 2\sigma_y \sigma_y + \sigma_z \sigma_z + 2\sigma_x \sigma_x + \sigma_y \sigma_y + \sigma_z \sigma_z) - 18\tau \vec{\sigma} \cdot \vec{\sigma}] \\
 &= \frac{\mu_0 \gamma_e^2}{4\pi r^3} \frac{1}{18\tau} [18\tau(\sigma_x \sigma_x + \sigma_y \sigma_y + \sigma_z \sigma_z) - 18\tau \vec{\sigma} \cdot \vec{\sigma}] \\
 &= 0.
 \end{aligned} \tag{4.10}$$

So during this 18τ period, the $e^- - e^-$ interaction averages to zero, which means the dipolar interaction is decoupled.

The approximated dipole-dipole interaction between two NV spins is shown as Eq. 3.18 which is of the same form as the electron-electron interaction. Therefore, the NV-NV interaction can also be decoupled by the same pulse sequence despite a different resonant frequency.

4.2.2 Hetero-spin Dipolar Interaction Recoupling with Mechanical Motion

When the 12-pulse sequences are applied on NV centers or electrons, the NV-NV or e^-e^- interactions will be decoupled. The NV- e^- dipolar interactions, shown in Eq. 3.13, will also be reduced by these pulse sequences when either of the two decoupling sequences is present:

$$\begin{aligned}\bar{H} &= \frac{\mu_0\gamma_e^2}{4\pi r^3} \frac{1}{18\tau} \tau (S_z\sigma_z - S_y\sigma_y + 2S_x\sigma_x + S_z\sigma_z + 2S_y\sigma_y + S_x\sigma_x - 2S_z\sigma_z \\ &\quad - S_x\sigma_x + 2S_y\sigma_y + S_z\sigma_z - 2S_x\sigma_x + S_y\sigma_y + S_z\sigma_z) \\ &= \frac{\mu_0\gamma_e^2}{4\pi r^3} \frac{1}{18} (5S_y\sigma_y + 2S_z\sigma_z)\end{aligned}\tag{4.11}$$

As seen in Eq. 4.11, the amplitude of $S_z\sigma_z$ term is reduced to 1/9. The NV- e^- coupling, especially the $S_z\sigma_z$ term, is necessary for transferring information between sample film electrons and NV centers on cantilever tips. To recouple the NV- e^- dipolar interaction, oscillation of the cantilever is introduced. With this motion, the distance between NV and e^- is time-dependent, so the NV- e^- interaction will not be affected as much under the pulse sequence.

The recoupled interaction is rescaled by a factor κ , which indicates how much the $S_z\sigma_z$ coupling is recoupled. Calculations of the scaling factor κ with different $\frac{\tau}{T_0}$ ratios were done, where $T_0 = \frac{1}{f_0}$ is the period of the oscillator.

As shown in Figure 4.3, when $18\tau = T_0$ or $2T_0$, κ reaches maximums, which indicates that the recoupling effect is optimized when the period of the 12-pulse sequence matches or doubles the oscillation period. Here, the period of the sequence is chosen to be the same as the oscillation period.

4.3 Experiment Procedure to Detect the Electron Dipolar Network with NVs with motion

As introduced in the above sections, we are able to decouple homo-spin dipolar interactions while recoupling the other interactions. Based on these techniques, a general experiment procedure is designed to probe the dipolar network among the electrons in the target film.

NV centers are initialized to the $m_s = 0$ ground state at the beginning of the experiment. In the first step, the electrons in the film are initialized to their ground state by using

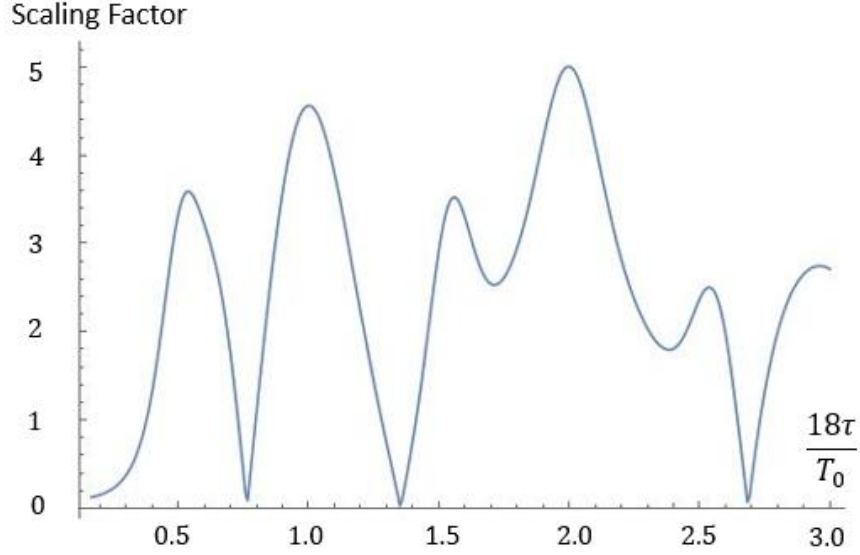


Figure 4.3: Scaling factor κ as a function of $\frac{18\tau}{T_0}$. κ is the ratio between the interaction strength with the mechanical motion present and absent.

NV centers. Dynamic nuclear polarization(DNP) method is expected to be used. To transfer the polarization from NVs to electrons the hetero-spin dipolar interactions should be present. The homo-spin dipolar interactions will not affect the polarizing procedure, so in this step, both kinds of dipolar interactions are kept.

In the second step, a Ramsey fringe experiment is applied on the target electron spins. Notice that the electrons should only evolve under the e^-e^- dipolar interaction, so in this step, the NV- e^- dipolar interaction needs to be decoupled while the e^-e^- is recoupled. The NV- e^- interaction can be decoupled if the $m_s \pm 1$ pseudo-spin- $\frac{1}{2}$ states can be manipulated, which requires the ability to generate transitions between NV $m_s = -1$ state and $m_s = +1$ state. The method to generate this transition at zero magnetic field will be demonstrated in Chapter 5.

In the third step, the state information of the electrons is transferred to the NV centers and indirectly measured by ODMR. To have a better resolution and remove the effects from surrounding spins, the homo-spin dipolar interactions are decoupled while keeping the hetero-spin interactions for information transfer.

By following the above steps, we are able to learn the average dipolar network of the small area that the tip with NVs is close to. To map the dipolar network in a larger film

area, we need to move the tip in the x-y plane and repeat those steps.

This experiment procedure still has many unsolved problems. The DNP method for the initialization process is one of the main concerns. Furthermore, the decoupling and recoupling processes are introduced in this chapter under the high field condition while the ideal case is to realize all the steps in the zero magnetic field. We are looking for the possible solutions for this problem. To start with, a method is demonstrated in Chapter 5 which enables us to achieve the NV state-selective transitions and hence realize the NV- e^- decoupling in the zero magnetic field.

Chapter 5

State-Selective Transitions in NV centers at Zero Field

The ground state of the NV center is a spin triplet state ($m_s = 0, \pm 1$). The transition between $m_s = \pm 1$ states is called double quantum transition (DQT) and the transition between $m_s = 0$ and $m_s = -1$ or $m_s = +1$ is called single quantum transition (SQT). DQT can be mediated by the $m_s = 0$ state. We represent the transition $m_s = +1 \leftrightarrow 0$ as π_+ , $m_s = -1 \leftrightarrow 0$ as π_- , and $m_s = +1 \leftrightarrow -1$ as $\pi_{\pm 1}$:

$$\pi_- = \begin{pmatrix} 0 & 1 & 0 \\ 1 & 0 & 0 \\ 0 & 0 & 1 \end{pmatrix}, \pi_+ = \begin{pmatrix} 1 & 0 & 0 \\ 0 & 0 & 1 \\ 0 & 1 & 0 \end{pmatrix}, \pi_{\pm 1} = \begin{pmatrix} 0 & 0 & 1 \\ 0 & 1 & 0 \\ 1 & 0 & 0 \end{pmatrix}. \quad (5.1)$$

Therefore, the DQT can be achieved by sandwiching three SQTs:

$$\pi_{\pm 1} = \pi_- \pi_+ \pi_-. \quad (5.2)$$

DQT has some special properties: the DQT frequency is more sensitive to the external field than SQT; $m_s = \pm 1$ can be used as a pseudo qubit. Therefore, control with high robustness of the $m_s = \pm 1$ manifold is especially important for NV centers as a magnetic sensor or a quantum computing qubit.

As introduced in Chapter 4, decoupling the NV- e^- dipolar interaction is important in the spin-mechanical sensor experiment design. DQT is a necessary part to realize such a decoupling. Moreover, a high magnetic field will introduce a spatial orientation and potential inhomogeneity to the system[52], which may reduce the resolution when we are relying on the spin-spin interaction as the sensing method. Therefore, DQT at zero magnetic field is

preferred for the spin-mechanical sensor proposed in Chapter 4. However, achieving DQT at the zero magnetic field is challenging due to the degenerate $m_s = \pm 1$ states. Starting from $m_s = 0$ state, $m_s = +1$ or $m_s = -1$ can not be selected specifically with linearly polarized microwave. Therefore, a state-selective SQT at zero field is required. In this chapter, the theoretical and experimental work on the high-fidelity control of the $m_s = \pm 1$ manifold at zero external magnetic field will be described.

5.1 Single Quantum Transition and Double Quantum Transition at Zero External Magnetic Field

At high external magnetic field, $m_s = \pm 1$ states are separate, and SQT can be achieved directly by applying linearly polarized microwave which is resonant with the energy gaps. However, to be sensitive to a weak magnetic source and remove the spatial orientation in the spectrum, zero external magnetic field is necessary. But at zero field, $m_s = +1$ and $m_s = -1$ states are degenerate. Starting from $m_s = 0$, the linearly polarized microwave can not select the state that the system evolves to. Instead it will take spins at $m_s = 1$ state to the superposition of $m_s = \pm 1$ states. In this case, a well-controlled circularly polarized microwave is necessary.

At zero magnetic field, the internal Hamiltonian of an NV^- center is

$$H_0 = \Delta S_z^2, \quad (5.3)$$

A non-linearly polarized microwave will be used instead of a linear one for control and the Hamiltonian is:

$$H_c(t) = \Omega_1 \cos(\omega t + \phi_1) S_x + \Omega_2 \cos(\omega t + \phi_2) S_y, \quad (5.4)$$

where $\omega = \Delta$ is the carrier frequency of the microwave, $\Omega_{1,2}$ are the envelope amplitudes and $\phi_{1,2}$ are the modulation phases.

The total Hamiltonian is $H_{tot} = H_0 + H_c(t)$. Going into the rotating frame of ΔS_z^2 , the rotated Hamiltonian is,

$$\begin{aligned}
\hat{H} &= e^{+i\Delta S_z^2 t} (H_{tot} - \Delta S_z^2) e^{-i\Delta S_z^2 t} \\
&= \frac{1}{2} (\Omega_1 \cos(\phi_1) S_x + \Omega_1 \sin(\phi_1) S'_y) + \frac{1}{2} (\Omega_2 \cos(\phi_2) S_y + \Omega_2 \sin(\phi_2) S'_x) \\
&= \frac{1}{2} \begin{pmatrix} 0 & \Omega_1 \cos(\phi_1) - \Omega_2 \sin(\phi_2) & 0 \\ \Omega_1 \cos(\phi_1) - \Omega_2 \sin(\phi_2) & 0 & \Omega_1 \cos(\phi_1) + \Omega_2 \sin(\phi_2) \\ 0 & \Omega_1 \cos(\phi_1) + \Omega_2 \sin(\phi_2) & 0 \end{pmatrix} \\
&\quad - \frac{i}{2} \begin{pmatrix} 0 & \Omega_1 \sin(\phi_1) + \Omega_2 \cos(\phi_2) & 0 \\ -\Omega_1 \sin(\phi_1) - \Omega_2 \cos(\phi_2) & 0 & \Omega_1 \sin(\phi_1) - \Omega_2 \cos(\phi_2) \\ 0 & -\Omega_1 \sin(\phi_1) + \Omega_2 \cos(\phi_2) & 0 \end{pmatrix}
\end{aligned} \tag{5.5}$$

where

$$S'_x = \frac{1}{\sqrt{2}} \begin{pmatrix} 0 & -1 & 0 \\ -1 & 0 & 1 \\ 0 & 1 & 0 \end{pmatrix}, S'_y = \frac{1}{\sqrt{2}} \begin{pmatrix} 0 & -i & 0 \\ i & 0 & i \\ 0 & -i & 0 \end{pmatrix}. \tag{5.6}$$

In ideal cases, $\Omega_1 = \Omega_2 = \Omega$, $\phi_1 = 0$, $\phi_2 = \frac{\pi}{2}$ (clockwise circularly polarized microwave), or $\phi_1 = 0$, $\phi_2 = -\frac{\pi}{2}$ (anti-clockwise circularly polarized microwave).

In the clockwise case,

$$\hat{H}_{cl} = \Omega \begin{pmatrix} 0 & 0 & 0 \\ 0 & 0 & 1 \\ 0 & 1 & 0 \end{pmatrix} \tag{5.7}$$

which gives the unitary that generates the $m_s = +1 \leftrightarrow 0$ transition,

$$U_{cl} = e^{-i\hat{H}_{cl}t} = \begin{pmatrix} 1 & 0 & 0 \\ 0 & 0 & e^{-i\Omega t} \\ 0 & e^{-i\Omega t} & 0 \end{pmatrix}. \tag{5.8}$$

In the anti-clockwise case,

$$\hat{H} = \Omega \begin{pmatrix} 0 & 1 & 0 \\ 1 & 0 & 0 \\ 0 & 0 & 0 \end{pmatrix} \tag{5.9}$$

which gives the unitary that generates the $m_s = -1 \leftrightarrow 0$ transition,

$$U_{anti-cl} = e^{-i\hat{H}_{anti-cl}t} = \begin{pmatrix} 0 & e^{-i\Omega t} & 0 \\ e^{-i\Omega t} & 0 & 0 \\ 0 & 0 & 1 \end{pmatrix}. \tag{5.10}$$

Therefore, DQT can be realized at zero field as well.

5.2 Enhance robustness with Optimal Control Theory

To achieve the state-selective transitions with high robustness, the parameters of the circularly-polarized microwave should be under strict control. However, the uncertainties in the experiment might affect the accuracy. The main uncertainty is the change of the NV center positions. In general cases, the position uncertainty is due to NV centers' natural drifts, but in the case considered in this thesis, the main cause is the mechanical motions of the tuning fork that the NV centers are attached to. Therefore, optimal control theory(OCT) is employed for realizing quantum gates that are robust to the uncertainty of the NV positions.

5.2.1 Generating Selective SQT at Zero Field using Two Parallel Wires

To generate the needed circularly polarized MW, instead of using only one wire which is to provide linearly polarized MW, two parallel wires are used as shown in Figure 5.1.

The magnetic field seen by the NV centers at (x_0, y_0) is determined by the current going

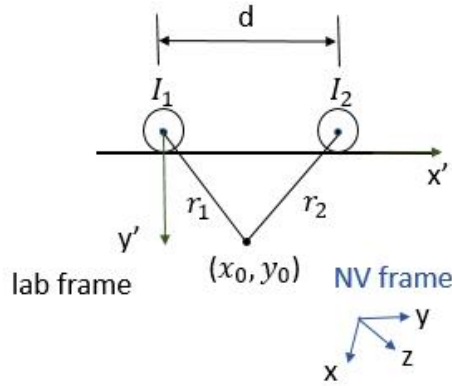


Figure 5.1: The two wires are separated by a distance d and have input currents I_1 and I_2 . The NV center is at (x_0, y_0) and is r_1 and r_2 away from the two wires. The magnetic field seen by the NV can be calculated in the NV center's principal axis frame.

through the two wires, $I_1(t)$ and $I_2(t)$, the distance d between the two wires, and the NV axis orientation. The Hamiltonian in the rotating frame of ωS_z^2 can be written as,

$$\tilde{H} = \frac{1}{2}(\Omega_{1x}S_x + \Omega_{1y}S_y + \Omega_{2x}S_{xp} + \Omega_{2y}S_{yp}) \quad (5.11)$$

where $(\Omega_{1x}, \Omega_{1y}, \Omega_{2x}, \Omega_{2y})$ are the control amplitudes and S_{xp}, S_{yp} are:

$$S_{xp} = \frac{1}{\sqrt{2}} \begin{pmatrix} 0 & -1 & 0 \\ -1 & 0 & 1 \\ 0 & 1 & 0 \end{pmatrix}, S_{yp} = \frac{i}{\sqrt{2}} \begin{pmatrix} 0 & -1 & 0 \\ 1 & 0 & 1 \\ 0 & -1 & 0 \end{pmatrix}. \quad (5.12)$$

Let the vectors $(n_{1x}, n_{1y}, 0)$ and $(n_{2x}, n_{2y}, 0)$ be the direction vectors in the NV frame along the magnetic fields generated by I_1 and I_2 , respectively.

The control amplitudes is subject to the relations below:

$$\begin{aligned} \Omega_{1x} &= c_{1x}n_{1x} + c_{2x}n_{2x}, \\ \Omega_{1y} &= c_{1y}n_{1y} + c_{2y}n_{2y}, \\ \Omega_{2x} &= -(c_{1y}n_{1x} + c_{2y}n_{2x}), \\ \Omega_{2y} &= -(c_{1x}n_{1y} + c_{2x}n_{2y}) \end{aligned} \quad (5.13)$$

where $\{c_{1x}, c_{1y}, c_{2x}, c_{2y}\}$ are

$$\begin{aligned} c_{1x} &= \frac{\gamma_e \mu_0}{4\pi} \frac{I_{1x}}{\sqrt{(x - \frac{d}{2})^2 + y^2}} \\ c_{1y} &= \frac{\gamma_e \mu_0}{4\pi} \frac{I_{1y}}{\sqrt{(x - \frac{d}{2})^2 + y^2}} \\ c_{2x} &= \frac{\gamma_e \mu_0}{4\pi} \frac{I_{2x}}{\sqrt{(x + \frac{d}{2})^2 + y^2}} \\ c_{2y} &= \frac{\gamma_e \mu_0}{4\pi} \frac{I_{2y}}{\sqrt{(x + \frac{d}{2})^2 + y^2}} \end{aligned} \quad (5.14)$$

Some particular directions are not allowed to ensure a full control on all the terms in Eq.5.11.

With the setup above, we want to generate a robust SQT gate that allows for small movement of the NV center by controlling the currents sent into the two wires. To achieve this, optimal control theory is needed.

5.2.2 Introduction to Optimal Control Theory and Gradient Ascent Algorithm

Optimal Control Theory (OCT)[54] is a modern dynamic optimizing method relying on differentiability and is broadly used in controllable systems. OCT uses control variables

for optimization which differs from Calculus of Variation.

In OCT, there are state variables $y(t)$, control variables $u(t)$ and target parameters V to be optimized. The control variables $u(t)$ need to be controllable and can affect the state variables of interest.

The basic goal of OCT is to find $u(t)$ that satisfies:

$$H(t, y, u^*) \geq H(t, y, u), \quad \forall t \in [0, T], \quad \forall u^* \neq u, \quad u, u^* \in \mathcal{U} \quad (5.15)$$

\mathcal{U} is a compact set of the control variable space.

In this thesis, an OCT technique named as gradient ascent pulse engineering (GRAPE)[\[55\]](#) is used to generate the target gate which is robust over multiple parameters.

In this numerical OCT algorithm, the goal is to achieve a target operator starting from an initial state.

The state of the spin system is $\rho(t)$. The motion of $\rho(t)$ is characterized by the equation:

$$\dot{\rho}(t) = -i[(H_0 + \sum_{k=1}^m u_k(t)H_k), \rho(t)], \quad (5.16)$$

where H_0 is the Hamiltonian of the system, H_k are the control Hamiltonians which are microwave pulses with controllable amplitudes u_k respectively. Given an initial state $\rho(0) = \rho_0$ and a target operator C , the goal of GRAPE is to fine optimal amplitudes $u_k(t)$ that maximize the overlap between the final state $\rho(T)$ and the target C . The overlap can be expressed as the inner product of C and $\rho(T)$:

$$\Phi_0 = \langle C | \rho(T) \rangle. \quad (5.17)$$

Discretize the time duration T into N steps:

$$T = N\Delta t, \quad (5.18)$$

and $u_k(j)$ is the control amplitude at the j^{th} time step. So the evolution at the j^{th} time step is

$$U_j = \exp \left[-i\Delta t \left(U_0 + \sum_{k=1}^m u_k(j)H_k \right) \right]. \quad (5.19)$$

The final state at $t = T$ is

$$\rho(T) = U_N \cdots U_1 \rho_0 U_1^\dagger \cdots U_N^\dagger \quad (5.20)$$

and the overlap is

$$\begin{aligned}
\Phi_0 &= \langle C | U_N \cdots U_1 \rho_0 U_1^\dagger \cdots U_N^\dagger \rangle \\
&= C^\dagger U_N \cdots U_1 \rho_0 U_1^\dagger \cdots U_N^\dagger \\
&= (U_j^\dagger \cdots U_N^\dagger) C^\dagger U_N \cdots U_1 \rho_0 U_1^\dagger \cdots U_N^\dagger (U_N \cdots U_j) \\
&= (U_j^\dagger \cdots U_N^\dagger C^\dagger U_N \cdots U_j) U_{j+1} \cdots U_1 \rho_0 U_1^\dagger \cdots U_{j+1}^\dagger (U_j^\dagger \cdots U_N^\dagger U_N \cdots U_j) \\
&= \lambda_j \rho_j
\end{aligned} \tag{5.21}$$

where λ_j is the backward propagated C at time j and ρ_j is the state at time j . Perturb $u_k(j)$ to $u_k(j) + \delta u_k(j)$, we have:

$$\delta U_j = -i \Delta t \delta u_k(j) \bar{H}_k U_j \tag{5.22}$$

where

$$\bar{H}_k = \frac{1}{\Delta} \int_0^{\Delta t} u_j(\tau) u_j(-\tau) d\tau. \tag{5.23}$$

Therefore,

$$\frac{\delta \Phi_0}{\delta u_k(j)} = - \langle \lambda_j | i \Delta t [H_k, \rho_j] \rangle \tag{5.24}$$

and we can update u_k to increase the overlap by

$$u_k(j) \rightarrow u_k(j) + \epsilon \frac{\delta \Phi_0}{\delta u_k(j)} \tag{5.25}$$

where ϵ is the size of a small step. In GRAPE algorithm, the steps to optimize the $u_k(j)$ is:

- (1) Assign $u_k(j)$ a initial guess;
- (2) From ρ_0 , calculate ρ_j for all $j \leq N$;
- (3) From C , calculate λ_j for all $j \leq N$;
- (4) Calculate $\frac{\delta \Phi_0}{\delta u_k(j)}$, and update the $m \times N$ control amplitude matrix $u_k(j)$ by Equation 5.25;
- (5) With new control amplitudes $u_k(j)$, go to step (2)

until Φ_0 satisfies the requirement set by the controller.

This algorithm promote the speed to find the optimal controls by decreasing the number of loops to 2 full-time evolution: ρ_0 from $0 \rightarrow T$ and λ_N from $N \rightarrow 0$. This speed-up enables the optimization for multiple experimental parameters.

5.2.3 Generating Selective SQT with High Robustness using GRAPE

To find the optimal pulse sequences, the well-written mathematica resource "QuantumUtils" is used. In the program, the target gate is set to be $\pi_{+1} = \begin{pmatrix} 1 & 0 & 0 \\ 0 & 0 & 1 \\ 0 & 1 & 0 \end{pmatrix}$.

The parameter distribution of (x, y) , which is the NV center position, is set to be a 2-dimensional Gaussian distribution in $[-5 \text{ nm}, 5 \text{ nm}] \times [-5 \text{ nm}, 5 \text{ nm}]$. The optimized pulse sequences can be found with fidelity over 99.5%. This fidelity is calculated by averaging over all the possible points (x, y) within the considered range. For the wire separation $d = 110 \text{ nm}$, the NV position $(10, 70) \mu\text{m}$ and a given NV principle axis orientation, the pulse sequences found and the corresponding robustness are plotted in Figure 5.2. In the robustness plot, it is shown that for most of the area, the fidelity is over 99.9%.

5.3 Experiment Design and Progress

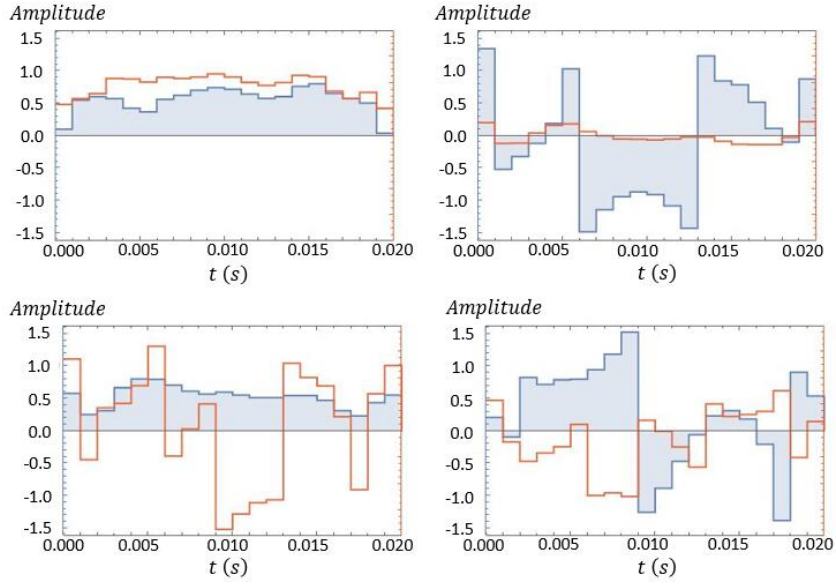
In this section, the experimental design, setup and progress for the state-selective SQT gate are introduced.

5.3.1 Experiment Procedure for Testing the State-selective SQT Gate

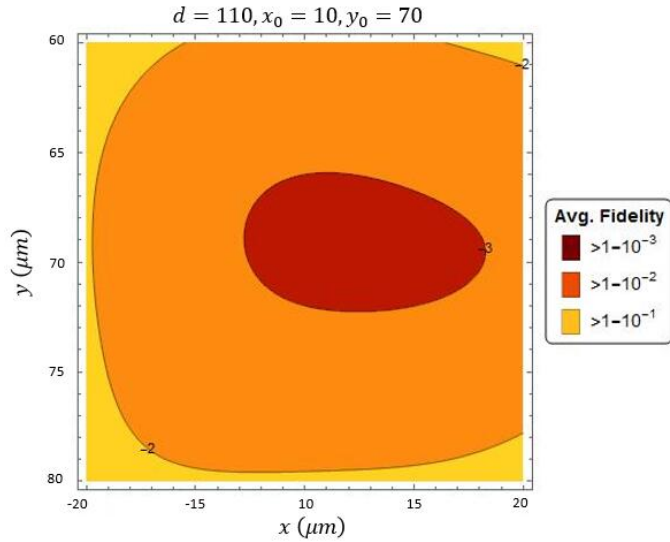
To implement the state-selective π_- gate and test whether it works, a procedure was designed as shown in Figure 5.3. A $e^{i\frac{\pi}{2}S_x}$ gate is followed by the π_- gate. After evolving the state under a small field B_z along z-axis for time τ' , apply $e^{-i\frac{\pi}{2}S_x}$ gate and observe.

If $\pi_{-1,0}$ operation is present, the final state will be

$$\begin{aligned} \psi_1 &= e^{-i\frac{\pi}{2}S_x} \cdot e^{-i\gamma B_z S_z \tau'} \cdot \frac{|0\rangle + |+1\rangle}{\sqrt{2}} \\ &= \frac{1}{2} \left(1 + \frac{ie^{-i\gamma B_z \tau'}}{\sqrt{2}} \right) |+1\rangle + \frac{1}{2} e^{-i\gamma B_z \tau'} |0\rangle + \frac{1}{2} \left(1 - \frac{ie^{i\gamma B_z \tau'}}{\sqrt{2}} \right) |-1\rangle \end{aligned} \quad (5.26)$$



(a)



(b)

Figure 5.2: The gray squares in (a) are the AWG output pulse sequences and the orange lines are same sequences transformed to the NV-axis frame. (b) is the corresponding robustness plot. Both (a) and (b) assume the two wires are separated by $110 \mu\text{m}$, and the NV location is at $(10 \mu\text{m}, 70 \mu\text{m})$. The dark orange part in the middle is the area where the gate has a fidelity over 99.9%.

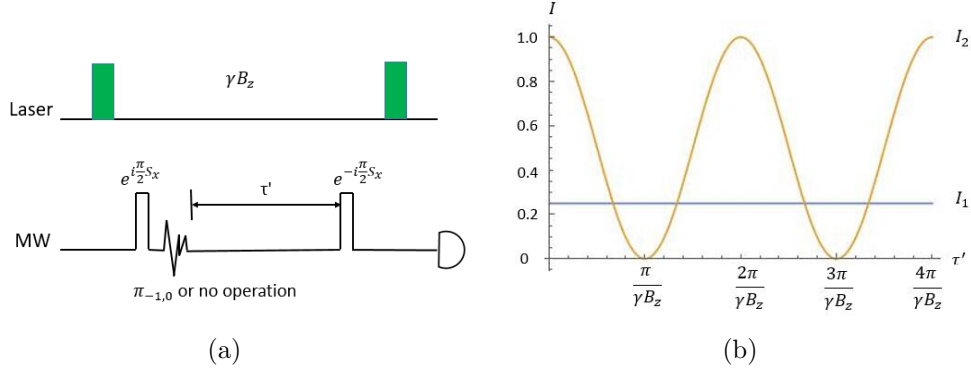


Figure 5.3: (a) Pulse sequences for the proving experiment. After initializing the NV centers with lasers, the MW pulse sequences is applied. The zigzag lines after the $e^{i\frac{\pi}{2}S_z}$ gate is the comparing experiment with or without the $\pi_{-1,0}$ transition.(b) Intensity vs τ' with or without the $\pi_{-1,0}$ transition

so the observed intensity is $I_1 = |\psi_1|^2 = \frac{1}{4}$.

If $\pi_{-1,0}$ operation is absent, the final state will be

$$\begin{aligned} \psi_2 &= e^{-i\frac{\pi}{2}S_x} \cdot e^{-i\gamma B_z S_z \tau'} \cdot \frac{|-1\rangle + |+1\rangle}{\sqrt{2}} i \\ &= \frac{1}{\sqrt{2}} \sin(\gamma B_z \tau') |+1\rangle + \cos(\gamma B_z \tau') |0\rangle - \frac{1}{\sqrt{2}} \sin(\gamma B_z \tau') |-1\rangle \end{aligned} \quad (5.27)$$

so the observed intensity is $I_2 = |\psi_2|^2 = \cos^2(\gamma_e B_z \tau')$.

Figure 5.3(b) is the intensity vs τ' plot. It is shown that with $\pi_{-1,0}$, the detected intensity I_1 is τ' -independent, but without π_{-} , the intensity I_2 is τ' -dependent and has a cosine shape. Therefore, whether the π_{-} gate is successful can be judged from the shapes of I_1 and I_2 .

5.3.2 Microwave circuits

A microwave circuit is designed to generate the proper currents that go into the parallel wires that are needed for the circularly polarized microwave. Arbitrary Wave Generator (AWG), attenuators, IQ mixers, amplifiers, synthesizers, power splitters, circulators and switches are important parts of this circuit. This circuit is shown in Figure 5.4.

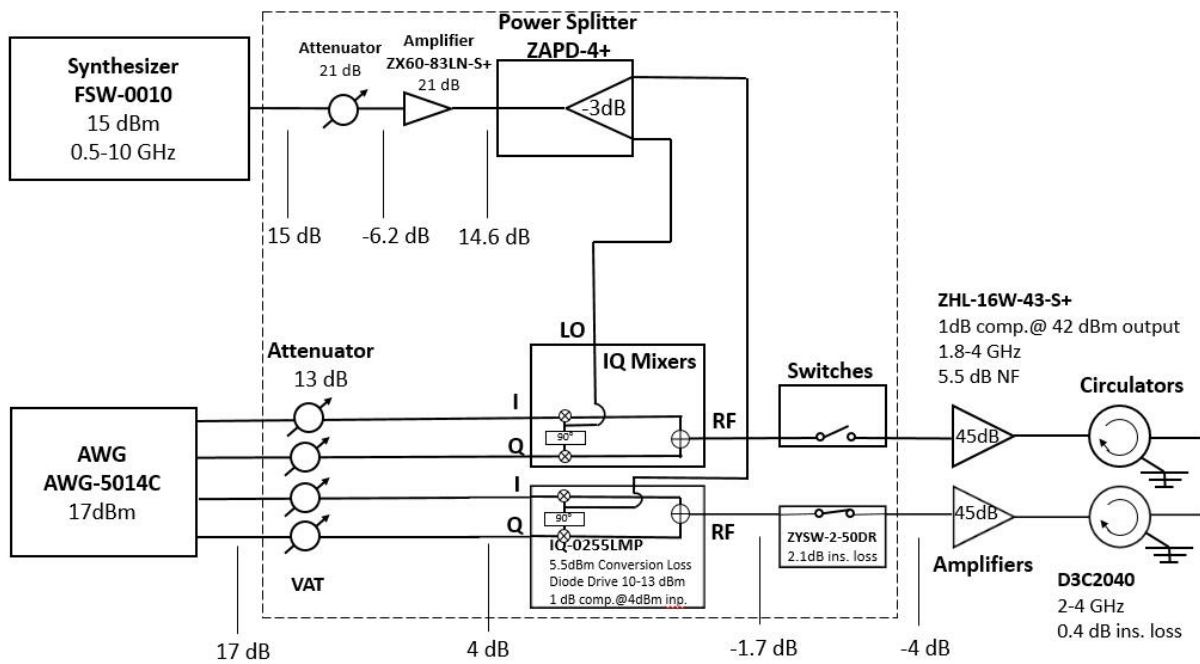


Figure 5.4: The design of the microwave circuit. The names and details about the circuit elements are labeled in the figure. The power loss and gain is estimated assuming that the insertion loss for each coax is 1 dB and for each adapter is 0.2 dB. The circuit part in the dashed box is place on a circuit board made by the author.

The electronics used in the circuit are briefly introduced below:

AWG-5014C

An arbitrary waveform generator (AWG) is used to generate repetitive or single-shot electric waveforms. In our circuit, a four-channel AWG-5014C is used.

IQ mixer

An IQ mixer is used together with a synthesizer to combine two current inputs to one current output with the frequency set by the synthesizer and the input currents. The phase and the amplitude of the output current is determined by the I, Q inputs α and β . As shown in Figure 5.4, the synthesizer connects to I, Q ports with a 90° phase shift. The two modulated currents are combined and output at RF port:

$$I(t) = \alpha \cos(\omega t) + \beta \sin(\omega t) = \sqrt{\alpha^2 + \beta^2} \cos(\omega t - \phi), \quad (5.28)$$

where

$$\phi = \arctan \frac{\beta}{\alpha}. \quad (5.29)$$

By controlling the amplitude α , β , we can control the current amplitude and phase we need for the microwave field.

Synthesizer

A synthesizer is an oscillator that generates electric signals at a chosen frequency. We use the FSW-0010 synthesizer which can generate the signal at frequency 0.5-10 GHz.

Power Splitter

Power splitters, also called power dividers, are directional electronics that accept one input and output multiple signals with certain phases and amplitudes. The power splitter used in the circuit divides the input into two outputs with a 0° phase difference.

Circulator

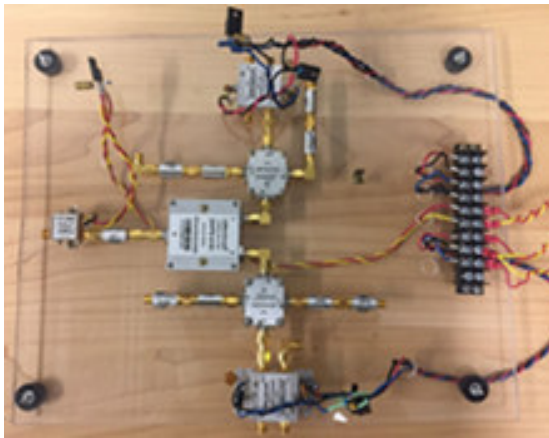
A circulator is a three- or four-port device. The microwave or radio frequency signal that enters one of the ports will output from the next port in a fixed order. In our microwave circuit, circulators can allow the currents in only one direction and prevent the currents in the opposite direction.

Amplifiers and Attenuators

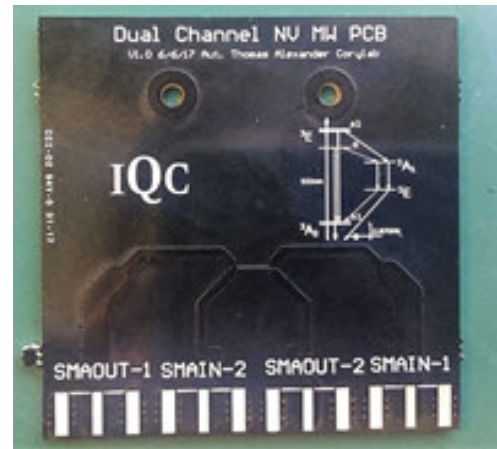
Amplifiers and attenuators are electronic devices that amplify or reduce the power of sig-

nals. They are included in the microwave circuit to control the power that enters some certain ports of other devices to meet their power requirements.

The microwave circuit board has been built as shown in Figure 5.5(a). The two circuits on the board that provide power for two wires have been tested separately by Romain Ruhlman and the author, and this circuit board works normally. The two parallel wires that generate the microwave are printed on a circuit board. It is called a printed circuit board (PCB). The sample PCBs are designed by Thomas Alexander and they have already been produced as shown in Figure 5.5(b). In the future, the diamond sample with NV centers need to be placed on top of the two wires on the PCB; the wires need to be connected to the microwave circuit board. After having every experimental component in place, the state-selective transition OCT pulse sequence can be tested experientially.



(a)



(b)

Figure 5.5: (a)The completed microwave circuit board. (b)The produced PCB with two parallel wires. The size of the board is designed to fit into the sample stage of the confocal microscopy.

Chapter 6

Summary and Future Work

In this thesis, the properties of NV centers and some basic experiments on NV centers are reviewed. A NV-based single-spin locating simulation is demonstrated with the help of machine learning technique. As the focus of the thesis, the scheme on building a spin-mechanical sensor for atomically thin films by using NV centers is proposed. To realize this scheme, different decoupling sequences for NV- e^- , e^-e^- and NV-NV dipolar interactions are developed. Especially, the state-selective transitions in NV centers at zero magnetic field with high fidelities are studied for the N- e^- decoupling purpose.

For the state-selective transition experiment, we have already made and tested the microwave circuit board and the PCB with the parallel wires as shown in Chapter 5. We are now putting every experimental element together to perform the proving experiment in the near future. When the state-selective SQT is successfully realized, the DQT at zero field should be applicable which is an important part of the spin-mechanical sensor.

However, there is still theoretic work that needs to be completed for the spin-mechanical sensor scheme. The dynamical nuclear polarization (DNP) is one of the most important parts. As has been mentioned, it is also hoped to complete all the work that has been done in Chapter 4 in the zero magnetic field environment to enhance the sensing sensitivity. When all these theoretical problems are solved, we can proceed to the study of this spin-mechanical sensor for practical applications.

References

- [1] S. Bogdanovi, S. B. van Dam, C. Bonato, L. C. Coenen, A. M. J. Zwerver, B. Hensen, M. S. Z. Liddy, T. Fink, A. Reiserer, M. Lonar, and R. Hanson. Design and low-temperature characterization of a tunable microcavity for diamond-based quantum networks. *Appl. Phys. Lett.* *110*, 171103 (2017).
- [2] O. Arcizet, V. Jacques, A. Siria, P. Poncharal, P. Vincent and S. Seidelin. A single nitrogen-vacancy defect coupled to a nanomechanical oscillator. *Nature Physics* *7*, 879883 (2011).
- [3] F. Dolde, H. Fedder, M. W. Doherty, T. Nbauer, F. Rempp, G. Balasubramanian, T. Wolf, F. Reinhard, L. C. L. Hollenberg, F. Jelezko and J. Wrachtrup. Electric-field sensing using single diamond spins. *Nature Physics* *7*, 459463 (2011).
- [4] L. M. Pham, D. Le Sage, P. L. Stanwix, T. K. Yeung, D. Glenn, A. Trifonov, P. Cappellaro, P. R. Hemmer, M. D. Lukin, H. Park, A. Yacoby and R. L. Walsworth. Magnetic field imaging with nitrogen-vacancy ensembles. *New Journal of Physics* *13* (2011) 045021.
- [5] N. Bar-Gill, L.M. Pham, A. Jarmola, D. Budker and R.L. Walsworth. Solid-state electronic spin coherence time approaching one second. *Nature Communications* *4* 1743 (2013).
- [6] F. Jelezko, T. Gaebel, I. Popa, M. Domhan, A. Gruber and J. Wrachtrup. Observation of coherent oscillation of a single nuclear spin and realization of a two-qubit conditional quantum gate. *Phys.Rev.Lett.* *93*(2004)130501.
- [7] F. Jelezko, T. Gaebel, I. Popa, A. Gruber, and J. Wrachtrup. Observation of Coherent Oscillations in a Single Electron Spin. *Phys.Rev.Lett.* *92*(2004)076401.

- [8] A. Gruber, A. Drbenstedt, C. Tietz, L. Fleury, J. Wrachtrup, C. von Borczyskowski. Scanning Confocal Optical Microscopy and Magnetic Resonance on Single Defect Centers. *Science* 27 (1997) Vol. 276, 5321, 2012-2014.
- [9] M. V. Gurudev Dutt, L. Childress¹, L. Jiang, E. Togan, J. Maze, F. Jelezko, A. S. Zibrov, P. R. Hemmer, M. D. Lukin. Quantum Register Based on Individual Electronic and Nuclear Spin Qubits in Diamond. *Science* 316(2007)1312.
- [10] P. Neumann, N. Mizuochi, F. Rempp, P. Hemmer, H. Watanabe, S. Yamasaki, V. Jacques, T. Gaebel, F. Jelezko, J. Wrachtrup. Multipartite entanglement among single spins in diamond. *Science* 320(2008)1326.
- [11] P. Neumann, R. Kolesov, B. Naydenov, J. Beck, F. Rempp, M. Steiner, V. Jacques, G. Balasubramanian, M. L. Markham, D. J. Twitchen, S. Pezzagna, J. Meijer, J. Twamley, F. Jelezko and J. Wrachtrup. Quantum register based on coupled electron spins in a room-temperature solid. *Nature Physics* 6(2010)249.
- [12] E. Togan, Y. Chu, A. S. Trifonov, L. Jiang, J. Maze, L. Childress, M. V. G. Dutt, A. S. Srensen, P. R. Hemmer, A. S. Zibrov and M. D. Lukin. Quantum entanglement between an optical photon and a solid-state spin qubit. *Nature* 466(2010)730.
- [13] C. Santori, P. E. Barclay, K-M. C. Fu, R. G. Beausoleil, S. Spillane and M. Fisch. Nanophotonics for quantum optics using nitrogen-vacancy centers in diamond. *Nanotechnology* 21(2010)274008.
- [14] J. W. Zhou, P. F. Wang, F. Z. Shi, P. Huang, X. Kong, X. K. Xu, Q. Zhang, Z. X. Wang, X. Rong, J. F. Du. Quantum information processing and metrology with color centers in diamonds. *Front. Phys.*, 2014, 9(5): 587597.
- [15] J. Cramer, N. Kalb, M. A. Rol, B. Hensen, M. S. Blok, M. Markham, D. J. Twitchen, R. Hanson and T. H. Taminiau. Repeated quantum error correction on a continuously encoded qubit by real-time feedback. *Nature* 506, 204, *Nature Communication* 7, 11526
- [16] F. Kong, C. Y. Ju, Y. Liu, C. Lei, M. Q. Wang, X. Kong, P. F. Wang, P. Huang, Z. K. Li, F. Z. Shi, L. Jiang, and J. F. Du. Direct Measurement of Topological Numbers with Spins in Diamond. *Phys. Rev. Lett.* 117, 060503 (2016)
- [17] P.C. Maurer , G. Kucsko , C. Latta , L. Jiang , N.Y. Yao , S.D. Bennett , F. Pastawski , D. Hunger , N. Chisholm , M. Markham , D.J. Twitchen , J.I. Cirac , M. D. Lukin , *Science* 336, 1283 (2012).

- [18] C. A. Ryan, J. S. Hodges and D. G. Cory. Robust Decoupling Techniques to Extend Quantum Coherence in Diamond. *Phys. Rev. Lett.* *105*, 200402 (2010).
- [19] J. M. Taylor, P. Cappellaro, L. Childress, L. Jiang, D. Budker, P. R. Hemmer, A. Yacoby, R. Walsworth and M. D. Lukin. High-sensitivity diamond magnetometer with nanoscale resolution. *Nature Physics* *7*, 270 (2011).
- [20] N. Zhao, J. L. Hu, S-W. Ho, J. T. K. Wan and R. B. Liu. Atomic-scale magnetometry of distant nuclear spin clusters via nitrogen-vacancy spin in diamond. *Nature Nanotechnology* *6*, 242246 (2011).
- [21] V. M. Acosta, E. Bauch, M. P. Ledbetter, A. Waxman, L.-S. Bouchard and D. Budker. Temperature Dependence of the Nitrogen-Vacancy Magnetic Resonance in Diamond. *Phys. Rev. Lett.* *104*, 070801 (2010).
- [22] F. Dolde, H. Fedder, M. W. Doherty, T. Nbauer, F. Rempp, G. Balasubramanian, T. Wolf, F. Reinhard, L. C. L. Hollenberg, F. Jelezko and J. Wrachtrup. Electric-field sensing using single diamond spins. *naturePhysics* *5*(2011)243.
- [23] L Rondin, J-P Tetienne, T Hingant, J-F Roch, P Maletinsky and V Jacques. Magnetometry with nitrogen-vacancy defects in diamond. *Reports on Progress in Physics*, *77*, No. 5 (2014).
- [24] I. Lovchinsky, J. D. Sanchez-Yamagishi, E. K. Urbach, S. Choi, S. Fang, T. I. Andersen, K. Watanabe, T. Taniguchi, A. Bylinskii, E. Kaxiras, P. Kim, H. Park and M. D. Lukin. Magnetic resonance spectroscopy of an atomically thin material using a single-spin qubit. *Science* *355*, 503–507 (2017).
- [25] D. Vasyukov, Y. Anahory, L. Embon, D. Halbertal, J. Cuppens, L. Neeman, A. Finkler, Y. Segev, Y. Myasoedov, M. L. Rappaport, M. E. Huber and E. Zeldov. A scanning superconducting quantum interference device with single electron spin sensitivity. *Nature Nanotechnology* *8*, 639644 (2013).
- [26] Roland Wiesendanger. Spin mapping at the nanoscale and atomic scale. *Rev. Mod. Phys.* *81*.1495 (2009)
- [27] H. S. Park, J. S. Baskin and A. H. Zewail. 4D Lorentz Electron Microscopy Imaging: Magnetic Domain Wall Nucleation, Reversal, and Wave Velocity. *Nano. Lett.*, *2010*, *10* (9), pp 37963803.

- [28] C. L. Degen, M. Poggio H. J. Mamin, C. T. Rettner and D. Rugar. Nanoscale magnetic resonance imaging. *pnas.0812068106*
- [29] I. Lovchinsky, J. D. Sanchez-Yamagishi, E. K. Urbach, S. Choi, S. Fang, T. I. Andersen, K. Watanabe, T. Taniguchi, A. Bylinskii, E. Kaxiras, P. Kim, H. Park, M. D. Lukin. Magnetic resonance spectroscopy of an atomically thin material using a single-spin qubit. *Science* 355, 503507 (2017).
- [30] S. Suzuki, R. M. Pallares and H. Hibino. Growth of atomically thin hexagonal boron nitride films by diffusion through a metal film and precipitation. *J. Phys. D: Appl. Phys.* 45 (2012) 385304.
- [31] C. Peetla, A. Stine, and V. Labhasetwar. Biophysical interactions with model lipid membranes: applications in drug discovery and drug delivery. *Mol Pharm.* 2009 ; 6(5): 12641276.
- [32] T. W. Borneman, C. E. Granade, and D. G. Cory. Parallel Information Transfer in a Multinode Quantum Information Processor. *Phys. Rev. Lett.* 108, 140502 (2012).
- [33] M. S. Mirkamali and D. G. Cory. Using a mesoscopic system to generate entanglement. *US Patent App.* 15/328,769, 2015.
- [34] J. R. Rabeau, A. Stacey, A. Rabeau, S. Prawer, F. Jelezko, I. Mirza and J. Wrachtrup. Single Nitrogen Vacancy Centers in Chemical Vapor Deposited Diamond Nanocrystals. *Nano Lett.*, 2007, 7 (11), pp 34333437.
- [35] R. Kalish, C. Uzan-Saguy, B. Phiiosoph, V. Richter, j.p. Lagrange, E. Gheeraert, A. Deneuville, A.T. Collins. Nitrogen doping of diamond by ion implantation. *Diamond and Related Materials* 6 (1997), 24, pp 516-520.
- [36] P. Neumann, J. Beck, M. Steiner, F. Rempp, H. Fedder, P. R. Hemmer, J. Wrachtrup and F. Jelezko. Single-shot readout of a single nuclear spin. *Science* 329 (5991), 542-544 (2010).
- [37] L. Robledo, L. Childress, H. Bernien, B. Hensen, P. F. A. Alkemade and R. Hanson. High-fidelity projective readout of a solid-state spin quantum register. *Nature* 477, 574-578 (2011).
- [38] B. B. Buckley, G. D. Fuchs, L. C. Bassett and D. D. Awschalom. Spin-Light Coherence for Single-Spin Measurement and Control in Diamond. *Science* 330 (6008), 1212-1215. 2010

- [39] C. E. Granade, C. Ferrie, N. Wiebe and D. G. Cory. Robust online Hamiltonian learning, *New Journal of Physics* 14, (2012).
- [40] C. Ferrie, C. Granade, D. G. Cory. How to best sample a periodic probability distribution, or on the accuracy of Hamiltonian finding strategies. *arXiv:1110.3067v2*.
- [41] A. Hentschel, B. C. Sanders. Efficient Algorithm for Optimizing Adaptive Quantum Metrology Processes. *Phys. Rev. Lett.* 107, 233601 Published 30 November 2011
- [42] A. Hentschel, B. C. Sanders. Machine Learning for Precise Quantum Measurement. *Phys. Rev. Lett.* 104, 0636030 (2010)
- [43] Samuel, Arthur. Some Studies in Machine Learning Using the Game of Checkers. *IBM Journal of Research and Development.* 3 (3)(1959).
- [44] J. R. Koza, F. H. Bennett, D. Andre, M. A. Keane. Artificial Intelligence in Design 96. *Springer, Dordrecht.* pp. 151170(1996).
- [45] J. R. Maze, A Gali, E Togan, Y Chu, A Trifonov, E Kaxiras and M D Lukin. Properties of nitrogen-vacancy centers in diamond: the group theoretic approach. *New Journal of Physics* 13 (2011) 025025.
- [46] C. P. Slichter. Principles of Magnetic Resonance. *Springer-Verlag, 3rd edition, (1990)*.
- [47] V. Jacques, P. Neumann, J. Beck, M. Markham, D. Twitchen, J. Meijer, F. Kaiser, G. Balasubramanian, F. Jelezko, and J. Wrachtrup. Dynamic Polarization of Single Nuclear Spins by Optical Pumping of Nitrogen-Vacancy Color Centers in Diamond at Room Temperature. *Phys. Rev. Lett.* 102, 057403 (2009).
- [48] D. G. Cory, J. B. Mille and A. N. Garroway. Time-suspension multiple-pulse sequences: applications to solid-state imaging. *Journal of Magnetic Resonance* 90, 205-213 (1990).
- [49] U. Haeberlen and J. S. Waugh. Coherent Averaging Effects in Magnetic Resonance. *Phys. Rev.* 175, 453(1968).
- [50] P. Mansfield, M. J. Orchard, D. C. Stalker, and K. H. B. Richards. Symmetrized Multipulse Nuclear-Magnetic-Resonance Experiments in Solids: Measurement of the Chemical-Shift Shielding Tensor in Some Compounds. *Phys. Rev. B* 7, 90 (1973).
- [51] M. Minsky. Memoir on Inventing the Confocal Microscope. *Scanning*, 10:128138, 1988.

- [52] A. Bielecki and A. Pines. Pake Patterns from Zero to High Field. *Journal of Magnetic Resonance* 74,381-385 (1987).
- [53] M. M. Maricq. Application of average Hamiltonian theory to the NMR of solids. *Phys. Rev. B* 25, 6622 (1982).
- [54] J Werschnik and E. K. U. Gross. Quantum optimal control theory. *Journal of Physics B: Atomic, Molecular and Optical Physics* 40 R175.
- [55] N. Khanejaa, T. Reissb, C. Kehletb, T. Schulte-Herbrüggenb, S. J. Glaserb. Optimal control of coupled spin dynamics: design of NMR pulse sequences by gradient ascent algorithms. *Journal of Magnetic Resonance* 172 2(2005) pp 296-305.
- [56] J. C. Cordes. The secular approximation with dipole-dipole interaction. *Journal of Physics B: Atomic and Molecular Physics* 20 (1987) 1433-1441.
- [57] M. W. Doherty, N. B. Manson, P. Delaney, F. Jelezko, J. Wrachtrup, and L. C. L. Hollenberg. The nitrogen-vacancy colour centre in diamond. *Physics Reports*, 528(1):1 45, 2013.
- [58] R. Blume-Kohout. Hedged maximum likelihood estimation. *Phys. Rev. Lett.* 105, 200504 (2010).